

Real-time dynamics induced by quenches across the quantum critical points in gapless Fermi systems with a magnetic impurity

Christian Kleine, Julian Mußhoff, and Frithjof B. Anders
*Lehrstuhl für Theoretische Physik II, Technische Universität Dortmund,
 Otto-Hahn-Straße 4, 44221 Dortmund, Germany*

The energy-dependent scattering of fermions from a localized orbital at an energy-dependent rate $\Gamma(\varepsilon) \propto |\varepsilon|^r$ gives rise to quantum critical points (QCPs) in the pseudogap single-impurity Anderson model separating a local moment phase with an unscreened spin moment from a strong-coupling phase which slightly deviates from the screened phase of standard Kondo problem. Using the time-dependent numerical renormalization group (TD-NRG) approach we show that local dynamic properties always equilibrate towards a steady-state value even for quenches across the QCP but with systematic deviations from the thermal equilibrium depending on the distance to the critical coupling. Local non-equilibrium properties are presented for interaction quenches and hybridization quenches. We augment our numerical data by an analytical calculation that becomes exact at short times and find excellent agreement between the numerics and the analytical theory. For interaction quenches within the screened phase we find a universal function for the time-dependent local double occupancy. We trace back the discrepancy between our results and the data obtained by a time-dependent Gutzwiller variational approach to restrictions of the wave-function ansatz in the Gutzwiller theory: while the NRG ground states properly account for the formation of an extended spin moment which decouples from the system in the unscreened phase, the Gutzwiller ansatz only allows the formation of the spin moment on the local impurity orbital.

PACS numbers: 05.70.Ln, 72.15.Qm, 78.67.Hc

I. INTRODUCTION

The investigation of the real-time dynamics in quantum-impurity systems (QISs) is essential for our understanding of dissipation and decoherence in qubits and electronic transport through nanodevices. Such systems consist of a small subsystem comprising a finite number of degrees of freedom, interacting with an infinitely large environment of noninteracting particles.

Elzerman *et al.* [1] have reported the usage of gate-voltage pulses for a single-shot readout of the spin configuration of a single-electron transistor in a finite magnetic field. Such a system can be modeled by an Anderson impurity model [2] coupled to a noninteracting metallic host. While the normal single-impurity Anderson model (SIAM) has a well-established and rather simple phase diagram [3, 4], it can be viewed as a special case ($r = 0$) of a more general class of models [5–8] whose coupling function $\Gamma(\varepsilon)$ to the local impurity contains a pseudogap; i.e. $\Gamma(\varepsilon) \propto |\varepsilon|^r$. Withoff and Fradkin were the first to point out the existence of a critical coupling [9] using a perturbative renormalization group argument. This system exhibits a wide variety of different phases for $r > 0$. These phases are characterized by different fixed points whose properties and occurrence depend on the bath exponent r as well as on particle-hole symmetry or the absence of it. For $0 < r < 1/2$, there exists [5, 6, 10, 11] a critical coupling strength Γ_c governing the transition between a local moment (LM) phase for a weak coupling and a strong-coupling (SC) phase for a large coupling to the metallic host.

In this paper, we analyze the real-time dynamics of different quenches within the LM or the SC phase but

also quenches across the quantum critical point (QCP) from one to the other phase for the particle-hole symmetric pseudogap Anderson impurity model (pg-SIAM). We employ a recent extension of Wilson’s numerical renormalization group (NRG) [4, 12] to the nonequilibrium quench dynamics, the time-dependent NRG (TD-NRG) [13–15].

While the quench dynamics in the SIAM ($r = 0$) has been investigated [13] using the TD-NRG, the nonequilibrium dynamics in the pg-SIAM within and across the QCP has only recently been addressed by a time-dependent Gutzwiller ansatz [16]. Using this extension of the well-established variational Gutzwiller technique [17, 18] to nonequilibrium [16, 19, 20] it has been demonstrated that the pseudogap coupling function can yield nontrivial dynamics as a consequence of the diverse low-energy fixed points of the model [16].

The pg-SIAM has been extensively investigated in the context of Kondo impurities in unconventional superconductors [5–8, 10, 11] or in the context of defects in graphene sheets [21, 22]. Some of the low-energy properties of the fixed points have been worked out in detail [23–25] and it has been shown that the universality class of the fixed point changes with the coupling function exponent r .

One intriguing property of this model is the absence of the Kondo screening at low coupling strength [6, 9–11] while for a large coupling a SC fixed point is found but with an only partially screened moment for particle-hole symmetric models. The question arises how these orthogonal ground states of the different phases influence the real-time dynamics of a system driven out of equilibrium by a quantum quench.

Since an effective spin degree of freedom decouples from the impurity in the LM phase, this fixed point (FP) property is expected to have a strong influence on the steady-state formation and the thermalization when quenched into the LM phase. We will show, however, that an oversimplified picture does not hold and requires some modification.

In all our quenches we find a well-defined steady state at long times. The distance from the thermal equilibrium for the same final Hamiltonian serves as a measure for the degree of thermalization. While for quenches within the SC phase, the system thermalizes within the numerical accuracy of the TD-NRG [13–15], the deviations from the thermal equilibrium remain negligible even for quenches across the QCP very close to the QCP. The deviation appears to be a continuous function of the distance to the critical coupling.

A. Physical picture

The surprising finding of a well-defined steady state even for quenches across the QCP into the LM phase can be understood in terms of the known fixed point properties of the model. It has been already pointed out in Ref. [6] that the local thermodynamic properties such as double occupancy as well as the fractional local moment on the impurity are continuous across the QCP.

In the strong-coupling (SC) phase, the Kondo temperature T_K governing the excitations around the SC FP vanishes at the QCP and increases with increasing coupling to the pseudogap metallic host. The crossover scale T^* taking the role of T_K in the LM phase characterizes the excitations around the LM FP, decreases with increasing coupling and also vanishes at the QCP.

The associated length scales $\xi^* = v_F/T^*$ ($\xi_K = v_F/T_K$) – v_F being the average Fermi velocity of the host material – can be interpreted as estimate for the spatial extension of the decoupled local moment (or the Kondo singlet in the SC phase.) Only for a very large local Coulomb repulsion U , the crossover scale T^* becomes large indicating that the local moment is mainly formed closely to or on the impurity.

Bearing in mind these known equilibrium properties [6] of the model it becomes apparent that an ansatz for the ground state restricted to a local moment formation on the impurity site only, as used in the Gutzwiller approach [16, 17, 19, 20], significantly underestimates the critical coupling Γ_c . Then, the local moment formation can only occur in such an approach at much lower coupling Γ or much larger local Coulomb repulsion U compared to the solution provided by the NRG.

This has also a profound consequence for the observed real-time dynamics. Due to the extended nature of the decoupled local moment, the local observable still can explore a larger phase space of itinerant states and, therefore, shows signs of thermalization close to the QCP.

Reducing the size of the local moment by increasing

U away from the critical U_c will still yield a steady state whose asymptotic properties start to deviate significantly from the thermal expectation values: Due to the increase of the nondecaying fraction of the expectation value [26–28] the difference between the steady-state and the thermal expectation value increases in the LM phase.

This difference, however, will strongly depend on the matrix element of the operator with the decoupling degree of freedom (DOF). While for the local double occupancy as a measure for the local correlations we find an increasing deviation between the long-time steady-state value and the thermal expectation value, the energy flow into the hybridization energy seems to be unaffected when crossing over to the localized regime. It is a rather surprising finding that hybridization energy shows thermalization even in the LM phase, although it has been conjectured that the TD-NRG might have problems in describing properly the energy flow [29].

B. Plan of the paper

The main objective of this paper is to discuss the real-time dynamics of the pseudogap SIAM with respect to interaction and hybridization quenches within a given phase and across the quantum critical point.

To be more specific, we will introduce the model in Sec. II A and briefly the TD-NRG in Sec. II B. We continue with a short overview over the rich phase diagram in Sec. II C – a much more comprehensive review can be found in Refs. [6, 8] – in order to define the types of quenches that will be investigated in Sec. III, the main part of the paper.

For completeness and defining the parameter space, we present the known NRG phase diagram for the symmetric pg-SIAM and also discuss the differences between the NRG and the equilibrium Gutzwiller results in Sec. III A. We start with analyzing our data for interaction quenches, i.e. the sudden switching on the local Coulomb repulsion. For small U and finite hybridization, the system remains in the SC phase. In Sec. III B 1, we show that universality can be found for this type of quench with a U -independent time scale. Interaction quenches across the QCP are investigated in Sec. III B 2. We address the difference between equilibration and thermalization.

Section III C is devoted to the two types of hybridization quenches. We augment our TD-NRG results with a perturbative analysis – details can be found in the Appendix – and show an excellent agreement between the numerics and the analytics in Sec. III C 2. We also discuss the energy flow from the reservoir to the impurity after the quench in Sec. III C 3. We end the paper with a short conclusion.

II. THEORY

A. The pseudo-gap single impurity Anderson model (pg-SIAM)

We consider a magnetic impurity comprising a spin-degenerated level that is coupled to a single conduction band. The Hamiltonian consists of three parts: H_c accounts for the conduction band of noninteracting electrons

$$H_c = \sum_{\vec{k}\sigma} \varepsilon_{\vec{k}\sigma} c_{\vec{k}\sigma}^\dagger c_{\vec{k}\sigma} \quad (1)$$

where $c_{\vec{k}\sigma}$ annihilates an electron with energy $\varepsilon_{\vec{k}\sigma}$ and spin σ , H_{imp} models the magnetic impurity

$$H_{\text{imp}} = \sum_{\sigma} \varepsilon_{d\sigma} d_{\sigma}^\dagger d_{\sigma} + U n_{d\uparrow} n_{d\downarrow}, \quad (2)$$

where d_{σ}^\dagger creates an electron in the localized impurity orbital with spin σ , the energy $\varepsilon_{d\sigma} = \varepsilon_d - H\sigma$, H is the local magnetic field measured in unit of energy, and $U > 0$ denotes the Coulomb repulsion between two localized electrons with opposite spin. Hereby $n_{d\sigma} = d_{\sigma}^\dagger d_{\sigma}$ is the occupation operator of the level with spin σ . These two subsystems are coupled by the hybridization term

$$H_{\text{hyb}} = \sum_{\vec{k}\sigma} V_{\vec{k}} \left(c_{\vec{k}\sigma}^\dagger d_{\sigma} + d_{\sigma}^\dagger c_{\vec{k}\sigma} \right) \quad (3)$$

so that the full dynamics is given by $H = H_c + H_{\text{imp}} + H_{\text{hyb}}$.

It has been realized [5–7] that the dynamics of the magnetic impurity is fully determined by the coupling function

$$\Gamma_{\sigma}(\epsilon) = \pi \sum_{\vec{k}} V_{\vec{k}}^2 \delta(\epsilon - \varepsilon_{\vec{k}\sigma}) \quad (4)$$

which we will take as spin-independent in the following. In real materials such as d superconductors [8] or graphene sheets [22, 30, 31] $\Gamma(\epsilon)$ is a complicated function of energy. It turned out, however, that only the low-energy part of the spectrum close to the chemical potential is relevant for the structure of the low-energy fixed points. Ignoring the high-energy details, $\Gamma(\epsilon)$ is replaced by the particle-hole symmetric power-law form

$$\Gamma(\epsilon) = (r+1)\Gamma_0 \left| \frac{\epsilon}{D} \right|^r \Theta(D - |\epsilon|) \quad (5)$$

where the cutoff D defines the effective band width [5–11]. The normalization factor $(r+1)$ ensures that the integral over the coupling function,

$$\pi V_0^2 = \int d\varepsilon \Gamma(\varepsilon) = 2\Gamma_0 D, \quad (6)$$

remains independent of the bath exponent $r \geq 0$. The parameter Γ_0 serves as the energy scale of the problem

that turns into the standard charge fluctuation scale for a constant density of states ($r = 0$). While $r = 0$ and $r = 1$ are the prototypical experimental realizations, we take r as an arbitrary parameter of the model.

The particle-hole asymmetry is governed by the deviation of $\Delta\epsilon = 2\epsilon_d + U$ from zero energy. Unless otherwise stated, we focus only on the particle-hole symmetric case in this paper.

B. The time-dependent numerical renormalization group (TD-NRG)

In this work, we exploit the NRG approach [4, 12] for obtaining all thermodynamic properties of the pg-SIAM. The key idea of Wilson was to map the logarithmically discretized coupling function $\Gamma(\varepsilon)$ onto an effective semi-infinite tight-binding chain where the impurity is coupled only to the first chain link. The energy hierarchy is controlled by the discretization parameter $\Lambda > 1$, and the problem is solved by iterative diagonalization.

Due to the exponential growth of the Hilbert space, high-energy states are discarded after each iteration. Since the initial basis set is known, the set of all discarded states form a complete basis set [13, 14] and simultaneously serve as an approximate eigenbasis of the Hamiltonian governing the time evolution of the problem.

Then the time-dependent expectation value $\langle O(t) \rangle$ of a general local operator \hat{O} can be cast into the form

$$\langle O(t) \rangle = \sum_m \sum_{r,s}^{\text{trun}} \mathbf{e}^{it(E_r^m - E_s^m)} O_{r,s}^m \rho_{s,r}^{\text{red}}(m), \quad (7)$$

where E_r^m and E_s^m are the dimensionful NRG eigenenergies of the Hamiltonian $H_f = H(t > 0)$ at iteration $m \leq N$, $O_{r,s}^m$ is the matrix representation of \hat{O} at that iteration, and $\rho_{s,r}^{\text{red}}(m)$ is the reduced density matrix defined as

$$\rho_{s,r}^{\text{red}}(m) = \sum_e \langle s, e; m | \hat{\rho}_0 | r, e; m \rangle \quad (8)$$

where $\hat{\rho}_0$ is the initial density operator of the problem prior to the quench. The restricted sum over r and s in Eq. (7) requires that at least one of these states is discarded at iteration m .

Implementing the TD-NRG requires two NRG runs: one for the initial Hamiltonian $H_i = H(t < 0)$ to construct the initial density operator $\hat{\rho}_0$ of the system and one for H_f to obtain the approximate eigenbasis governing the time evolution in Eq. (7). For more details on the TD-NRG see Refs. [13, 14]. Recently, the TD-NRG has been extended to use the full density matrix including pulsed Hamiltonians [15] and periodic switching [32].

In the original implementation of the TD-NRG – see Eq. (42) in Ref. [14] – each phase factor in Eq. (7)

$$e^{it(E_r^m - E_s^m)} \rightarrow e^{it(E_r^m - E_s^m) - \Gamma_m t} \quad (9)$$

was Lorentz-broadened with an energy-resolution-dependent damping factor $\Gamma_m = \alpha\omega_m$ proportional to the energy scale $\omega_m = D\Lambda^{-(m-1)/2}(1+1/\Lambda)/2$ at iteration m for all $E_r^m - E_s^m \neq 0$, and $\alpha = O(1)$ see Ref. [13, 14] for details. Such a broadening smoothenes the discretization-related oscillations in the same spirit as the broadening of the NRG Lehmann representation of equilibrium spectral functions [4, 33, 34]. If, however, localized states decoupled from the continuum contribute to the expectation value as discussed in the local moment phase of the model [6, 16], such a broadening could wrongly damp out oscillatory contributions at long times. In order to avoid any prejudice, we usually set $\alpha = 0$ and use the z averaging to minimize discretization-related oscillations. Therefore, usually all our data contain some finite-size-related noise at very long times. In order to illustrate the effect of the original TD-NRG broadening, we have used $\alpha = 0.4$ in Fig. 13(c) and $\alpha = 1$ in Fig. 14 instead of z averaging.

C. Overview of the phases and the quench types

The equilibrium phase diagram of the pg-SIAM is very rich and has been carefully explored by Gonzalez-Buxton and Ingersent [6]. Details can also be found in Refs. [8] and [4].

For a particle-hole (ph) symmetric model, an unstable intermediate coupling fixed point governs the transition between the local moment (LM) fixed point (FP) and the strong-coupling (SC) FP for $0 < r < 1/2$, where the critical coupling ratio U_c/Γ_0 depends on the band width D and the exponent r . The intermediate FP is also unstable with respect to ph-symmetry breaking since potential scattering is a marginally relevant perturbation at this FP.

In contrast to the standard SC FP for $r = 0$, the SC FP of the ph-symmetric pg-SIAM is characterized by a residual impurity entropy $S_{\text{imp}} = 2rk_B \ln(2)$ and a residual unscreened effective local moment [6] of $\mu_{\text{eff}}^2(0) = \lim_{T \rightarrow 0} \mu_{\text{eff}}^2(T) = r/8$.

For $1/2 < r$ the low-energy density of states is too small to screen the local spin, and only the LM FP remains stable for all coupling strengths at ph symmetry. Breaking ph symmetry, an asymmetric SC (ASC) fixed point is found for all r . Its thermodynamic properties are closely related to the standard $r = 0$ SC FP since $S_{\text{imp}} = 0$ and $\mu_{\text{eff}}^2(0) = 0$.

In addition, a second intermediate coupling fixed point at a finite value of the potential scattering is found for $r^* \approx 0.375 < r$, where the perturbation $V - V_c$ with respect to the critical potential scattering V_c is a marginal irrelevant operator [6].

In this paper, however, we will focus on the non-equilibrium dynamics of the particle-hole symmetric model close to and across the quantum-phase transition. Therefore, we mainly focus on the parameter regime $0 < r < 1/2$. There are two different ways to drive the

ph-symmetric system across the quantum critical point (QCP) for $0 < r < 1/2$. For a fixed value of U we can vary the hybridization strength Γ_0 , which will be called hybridization quench (HQ) in the following, or for a fixed Γ_0 we can change U that defines the interaction quench (IQ). In Table I we summarize our notation for the different quench types. The naming of the phases refers to the equilibrium low-temperature FP of the final Hamiltonian H_f after the quench.

In equilibrium, the SC FP can be reached in two ways: choosing the charge-fluctuation scale $\Gamma_0 > \Gamma_c(U)$ for fixed U or by setting $U < U_c(\Gamma_0)$ for fixed Γ_0 . The resulting phase diagram for $U_c(r)$ and $\Gamma_c(r)$ for fixed Γ_0 and U respectively is shown in Fig. 1(b). The details of how the phase diagram is obtained from equilibrium NRG calculations is presented in Sec. III A below.

An approximative description of the ground state wave function of the model for a finite hybridization has been proposed using a Gutzwiller wave-function ansatz [16]. For $r = 0$, the quasiparticle renormalization factor $Z \propto T_K^G \propto \exp(-\pi U/16\Gamma_0)$ is a smooth function of the Coulomb interaction U and has been interpreted as effective Kondo temperature within the Gutzwiller approach [17]. Note, however, that (i) the exponent differs by a factor of 2 from the standard Kondo temperature and, therefore, underestimates the exponential decay [35] and (ii) an incorrect Kondo scale is found for the wide-band limit as has been pointed out in Ref. [35].

For $r > 0$, a finite critical U_c and a QCP is found [16] for all r . The prediction for U_c by the Gutzwiller approach has been added to Fig. 1(b) as an analytical curve for the wide-band limit. That restricts the possible validity of the Gutzwiller approach to $r < 1/2$ since for $1/2 < r$ the LM FP is stable for all $U > 0$. The prediction of a SC phase even for $1/2 < r$ by the Gutzwiller approach is directly related to the restriction of the wave function to the formation of a decoupled spin moment on the impurity site while the true ground state properly accounts for the formation of an extended spin moment as we will discuss in the next section. The comparison with the correct NRG phase boundary reveals again an underestimation of the renormalization effects and, hence, an overestimation of the critical U_c . We have to bare in mind these limitations of the Gutzwiller approach of the equilibrium when comparing recent results [16] obtained with a time-dependent Gutzwiller approach [19, 20] with our TD-NRG data.

III. RESULTS

We begin with a short review of the established thermodynamic properties in Sec. III A and discuss the differences between the NRG findings [6] and the predictions of the equilibrium Gutzwiller ansatz. Then we proceed with the results of our TD-NRG calculations for interaction quenches (IQs) in Sec. III B and for hybridization quenches (HQs) in Sec. III C.

TABLE I. Summary of the quench types. The critical parameters Γ_c and U_c are r dependent and presented in Fig. 1. The phase type refers to the low-temperature FP of the final Hamiltonian. The numerical values of the critical parameters for different band widths D and exponents r are given in Table II.

Phase	Hybridization Quench	Interaction Quench
SC	$\Gamma_0 > \Gamma_c(U)$	$U < U_c(\Gamma_0)$
LM	$\Gamma_0 < \Gamma_c(U)$	$U > U_c(\Gamma_0)$

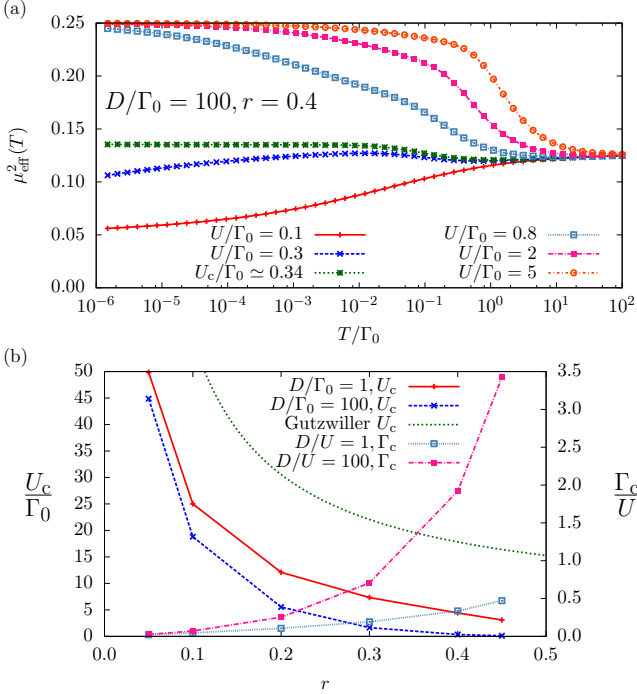


FIG. 1. (Color online) (a) Effective magnetic moment for different Coulomb interactions U with $D/\Gamma_0 = 100$ and $r = 0.4$. The critical parameter for this setup is $U_c/\Gamma_0 = 0.3392$. (b) Phase diagram for different bath exponents r and bandwidths D . For comparison the analytical form of the Gutzwiller ansatz (cf. Ref. [16]) is added.

A. Equilibrium properties

In order to set the stage for the real-time dynamics, we extend the review of the equilibrium properties to the temperature-dependent impurity observables [4, 6, 8].

One important quantity revealing the QCP is the effective local moment

$$\mu_{\text{eff}}^2(T) = \Delta \left(\langle S_z^2(T) \rangle - \langle S_z(T) \rangle^2 \right) \quad (10)$$

whereby $\Delta(X)$ is measuring the observable X in the presence of the impurity and the Wilson chain and subtracts the effect of the quantity X of the pure Wilson chain without the impurity at temperature T , and S_z denotes the z component of the total spin of the system. By this

definition [6, 12] the impurity contribution of the quantity X is extracted.

Note, however, that $\mu_{\text{eff}}^2(T)$ does not measure the local impurity spin observable but rather the difference in the total system properties with and without the impurity. Hence, the effective impurity spin momentum $\mu_{\text{eff}}^2(T)$ is in general related to a degree of freedom (DOF) comprising a linear combination of local and conduction electron spin observables. This will become important for understanding the impurity expectation values in the different phases.

In the LM FP, the effective local moment of the impurity spin, i.e., $\mu_{\text{eff}}^2(0) = \lim_{T \rightarrow 0} \mu_{\text{eff}}^2(T)$, is given by those of the free spin 1/4 while for the symmetric SC FP a residual moment $r/8$ has been found [6] revealing the inability of a power-law density of states to completely screen the Kondo spin.

In Fig. 1(a), $\mu_{\text{eff}}^2(T)$ is shown as function of temperature for different Coulomb interactions U for the bath exponent $r = 0.4$ with the band width $D/\Gamma_0 = 100$. If not mentioned otherwise we used the NRG parameter [12] $\Lambda = 2$ and kept $N_S = 2000$ states after each iteration step.

For $U/U_c < 1$ the effective local moment $\mu_{\text{eff}}^2(T)$ declines at low temperatures towards the SC FP value $r/8$ whereas for $U/U_c > 1$ it inclines towards 1/4 indicating a free local moment of the LM FP. For $U/\Gamma_0 = 0.34 \approx U_c$, $\mu_{\text{eff}}^2(T)$ approaches the value of the unstable intermediate coupling FP. We used the clear distinction between $\mu_{\text{eff}}^2(T)$ of the symmetric SC FP and the LM FP to define the critical Coulomb interaction U_c at which the value of the intermediate coupling FP is obtained.

In Fig. 1(b) we present the phase diagram of the p-symmetric pg-SIAM defined by the critical parameter U_c (or Γ_c respectively) for different bandwidths D . The numerical values of the critical parameters are given in Table II. We observe a strong influence of the band width D onto the critical U_c , and our Γ_c agrees excellently with Fig. 5 in Ref. [6].

In order to qualitatively understand the phase diagram in Fig. 1(b), we start from $U = 0$, where we always find a SC FP for $r < 1/2$. Since we systematically eliminate the high-energy degrees in a RG procedure, a finite U will matter only once the effective band width $D \rightarrow D_{\text{eff}}$ has reached the order U . At those energies, the system starts detecting the differences between the local doubly occupied state and the local moment states, and the effective coupling to the remaining conduction band is given by $\Gamma(U)$. Since $\Gamma(U)$ decreases with increasing r and increasing D , U_c also must decrease.

From the NRG calculation of the local moment as depicted in Fig. 1(a) it is apparent that the approach to the LM FP close to the QCP is governed by a small energy scale T^* vanishing at U_c [36]. Consequently all energy scales contribute to the local moment formation in the LM phase close to U_c , similar to estimated dimension of the Kondo cloud by $\xi_K = v_F/T_K$ in the SC phase [37–42]. Therefore, we interpret $\xi^* \propto v_F/T^*$ as an estimate

TABLE II. Summary of the critical parameters $U_c(\Gamma_0)$ and $\Gamma_c(U)$ as they are presented in Fig. 1.

r	$\frac{U_c}{\Gamma_0}; \frac{D}{\Gamma_0} = 1$	$\frac{U_c}{\Gamma_0}; \frac{D}{\Gamma_0} = 100$	$\frac{\Gamma_c}{U}; \frac{D}{U} = 1$	$\frac{\Gamma_c}{U}; \frac{D}{U} = 100$
0.05	49.84	44.87	0.02154	0.0268
0.1	25.00	18.81	0.04586	0.07094
0.2	12.10	5.534	0.10637	0.2535
0.3	7.331	1.6414	0.19246	0.7060
0.4	4.426	0.3392	0.3358	1.918
0.45	3.0826	0.1075	0.4724	3.423

for the spatial extension of the local moment decoupling from a free conduction band.

Additionally we have included the analytical prediction for the critical Coulomb interaction $U_c/\Gamma_0 = 16(r+1)/(\pi r)$ derived by a Gutzwiller ansatz [20] for the pg-SIAM [16] into Fig. 1(b). The Gutzwiller approach systematically overestimates U_c since its wave-function ansatz is trying to strictly enforce a formation of the free local moment on the impurity in the LM phase. Such a picture is only valid for very large U for that the system is already deeply located in the LM phase. The Gutzwiller ansatz has two shortcomings: (i) it overestimates the critical U_c and, therefore, the SC regime since it cannot describe an extended local moment formation and (ii) the local impurity decouples completely from the conduction band in the LM phase which will have profound consequences for the real-time dynamics within such an approach.

Since we investigate the real-time dynamics of the double occupancy $\langle D(t) \rangle$ for different type of quenches, we also provide results for the equilibrium double occupancy $\langle D \rangle_{\text{eq}}$ vs U/Γ_0 at fixed $D/\Gamma_0 = 100$ in Fig. 2. The NRG data depicted in Fig. 2(a) demonstrates that $\langle D \rangle_{\text{eq}}$ is continuous across the QCP. This continuity of local observables across the QCP was already pointed out by Gonzalez-Buxton and Ingersent more the 15 years ago – see Fig. 8 in Ref. [6]. We also added Gutzwiller equilibrium data calculated for the same hybridization function $\Gamma(\epsilon)$ as Fig. 2(b) to illustrate the difference to the NRG. Within the Gutzwiller ansatz, $\langle D(U_c) \rangle_{\text{eq}} = 0$ and remains zero for $U > U_c$. Consequently, the physical properties of the Gutzwiller wave function deviate significantly from the true ground state as obtained by the NRG. Apparently, the Gutzwiller wave function ansatz cannot be applied in the LM phase close to the QCP since it misses the spatial extension of the local moment that is decoupling from the system.

B. Interaction quenches

In an interaction quench, we switch the Coulomb repulsion from its initial value U_i at times $t < 0$ to the value U_f for $0 \leq t$. In order to maintain ph symmetry at all

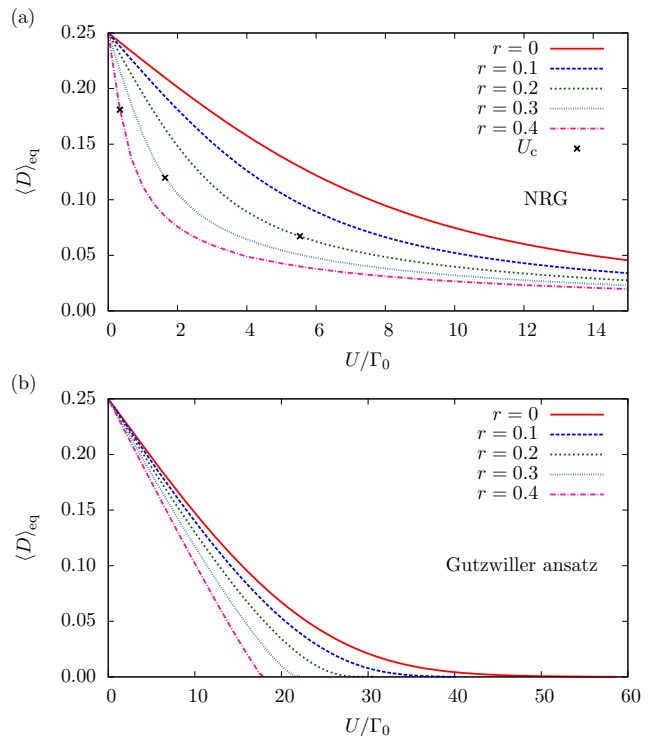


FIG. 2. (Color online) Equilibrium expectation value of the double occupancy $\langle D \rangle_{\text{eq}}$ versus U for different bath exponents r and $D/\Gamma_0 = 100$ calculated (a) using the equilibrium NRG and (b) using the equilibrium Gutzwiller ansatz [16, 20].

times, i.e. $U(t) + 2\epsilon_d(t) = 0$, we enforce also a switching in the d -level energy $-2\epsilon_d(t) = \Theta(-t)U_i + \Theta(t)U_f$. The hybridization strength $\Gamma(t) = \Gamma_i = \Gamma_f = \Gamma_0$ is kept constant and is used as a unit of energy. Short, intermediate, and long times will correspond to $t\Gamma_0 \ll 1$, $t\Gamma_0 \sim 1$ and $t\Gamma_0 \gg 1$.

We prepare the system initially in the uncorrelated state by setting $U_i = \epsilon_i = 0$. Since the impurity is coupled to the conduction band, the system approaches the SC FP for $T \rightarrow 0$. Therefore, the initial double occupancy is given by the uncorrelated value $\langle D \rangle_{\text{eq}} = 1/4$. In the LM FP, the double and the empty states on the magnetic impurity remain unoccupied, and $\langle D \rangle_{\text{eq}} = 0$.

1. Quenches within the SC phase

For switching on the Coulomb repulsion at $t = 0$, we can distinguish two cases: (i) for $U_f < U_c$ the system remains in the SC phase while (ii) for $U_f > U_c$ the equilibrium properties of the quenched system belong to the LM phase. Since we maintain ph symmetry, the local occupancy always remains at half filling and is unaffected by the quench. Therefore, we focus on the dynamics of the local double occupancy $\langle D(t) \rangle$. For a clear energy separation of band width D and charge fluctuation scale Γ_0 , we have chosen $D/\Gamma_0 = 10, 100 \gg 1$.

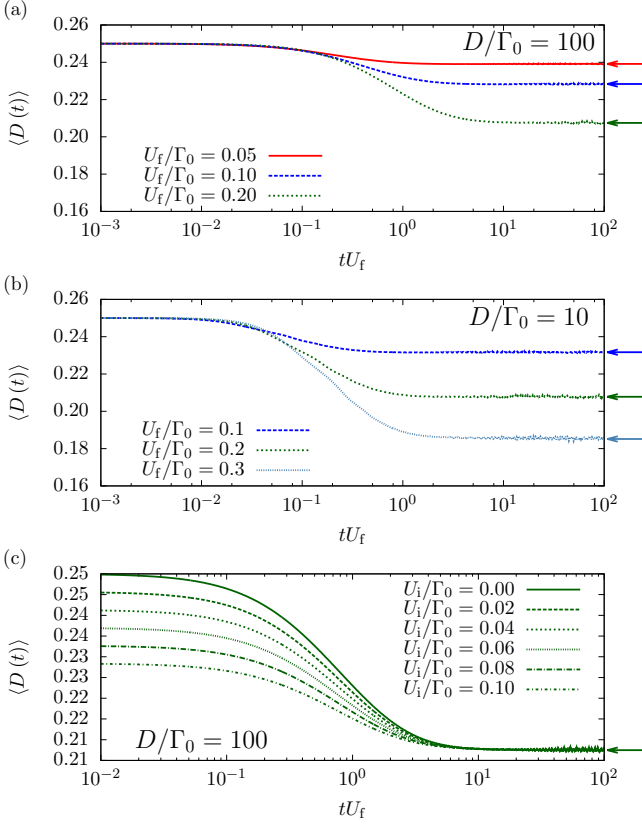


FIG. 3. (Color online) Time-dependent expectation value of the double occupancy $\langle D(t) \rangle$ for quenches within the SC phase. As a guide to the eye the equilibrium expectation values after the quench are marked by the arrows at the right side of the graph. (a) For the wide band $D/\Gamma_0 = 100$ with Coulomb repulsions $U_f/\Gamma_0 = 0.05, 0.1, 0.2 < U_c/\Gamma_0 \simeq 0.34$, (b) for $D/\Gamma_0 = 10$ with Coulomb repulsions $U_f/\Gamma_0 = 0.1, 0.2, 0.3 < U_c/\Gamma_0 \simeq 1.51$. For both bandwidths the system thermalizes at long times to its equilibrium value. (c) $\langle D(t) \rangle$ for different values of U_i and $U_f/\Gamma_0 = 0.2$.

In Fig. 3 we present the time-dependent local double occupancy $\langle D(t) \rangle$ for quenches within the SC phase, $U_f < U_c$, for two different band widths D for $r = 0.4$. All curves start at the non-interacting value $\langle D(t=0) \rangle = 1/4$ and reduced to smaller values since the Coulomb interaction is suppressing the charge fluctuations and the local double occupancy.

Quenches within the SC phase thermalize at long times to the equilibrium value of the quenched system. This thermalization is independent of the initial value U_i as shown in Fig. 3(c). The equilibrium values obtained from an independent equilibrium NRG calculation are indicated as arrows on the right side of the graph. The decay is governed by the time scale set by the charge fluctuation scale Γ_0 . In contrary to results [16] obtained by a time-dependent Gutzwiller ansatz – see Fig. 2 in Ref. [16] – we do not find any oscillations in the double occupancy. However, the time-dependent Gutzwiller approach predicts the thermalization of $\langle D(t) \rangle$ for those

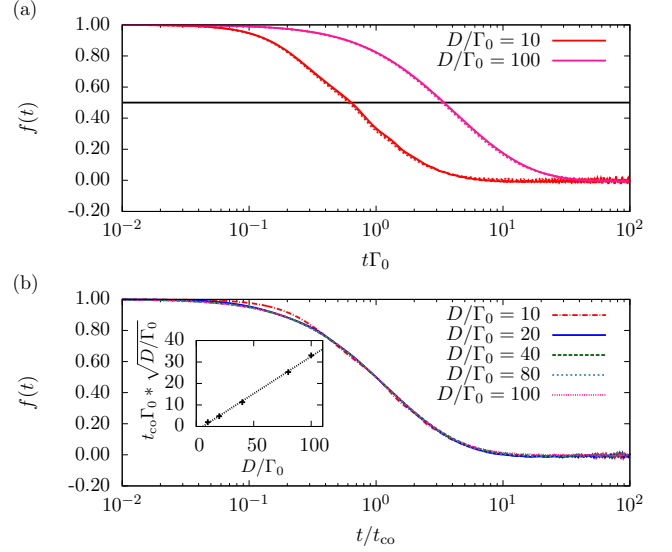


FIG. 4. (Color online) Scaling function $f(t)$ defined in Eq. 11 versus t : (a) using the data of Fig. 3 for different U_f , (b) $f(t)$ versus t/t_{co} for different bandwidths. The inset in (b) shows the time scale t_{co} in dependence of the bandwidth D .

type of quenches [16] which is a non-trivial result.

It is interesting to note that we find universality for interaction quenches within the SC phase. In order to eliminate the influence of the different long-time expectation values of $\langle D(t \rightarrow \infty) \rangle$ that includes the U_f dependency, we define the function

$$f(t) = \frac{\langle D(t) \rangle - \langle D(\infty) \rangle}{\langle D(0) \rangle - \langle D(\infty) \rangle} \quad (11)$$

of the time-dependent double occupancy $\langle D(t) \rangle$. The function f starts at $f(0) = 1$ and approaches $f = 0$ at infinitely long times independent of the parameters.

In Fig. 4(a) we demonstrate that all data depicted in Fig. 3 collapse onto one universal curve that is only dependent on the ratio D/Γ_0 . To eliminate the Γ_0 dependency, we define a crossover time t_{co} as $f(t_{co}) = 0.5$. Plotting $f(t)$ versus the dimensionless time scale t/t_{co} maps all data for different ratios D/Γ_0 onto one unique curve, depicted in Fig. 4(b). Only the curve for $D/\Gamma_0 = 10$ deviates slightly from the others: In this case the separation of energy scales is much less pronounced. The inset of Fig. 4(b) illustrates the dependency of t_{co} on D/Γ_0 . By fitting the numerical data we find that

$$t_{co} \propto \frac{1}{\Gamma_0} \sqrt{\frac{D}{\Gamma_0}} \quad (12)$$

This establishes universality in the $f(t)$ dynamics: the U_f dependency enters only via $\langle D(\infty) \rangle$ while the remaining real-time dynamics is only governed by the time scale t_{co} which depends on D and Γ_0 .

So far, we only used a fixed bath exponent $r = 0.4$. We extended our investigation to interaction quenches within the SC phase to $r = 0, 0.1, 0.2, 0.3$. Again, we

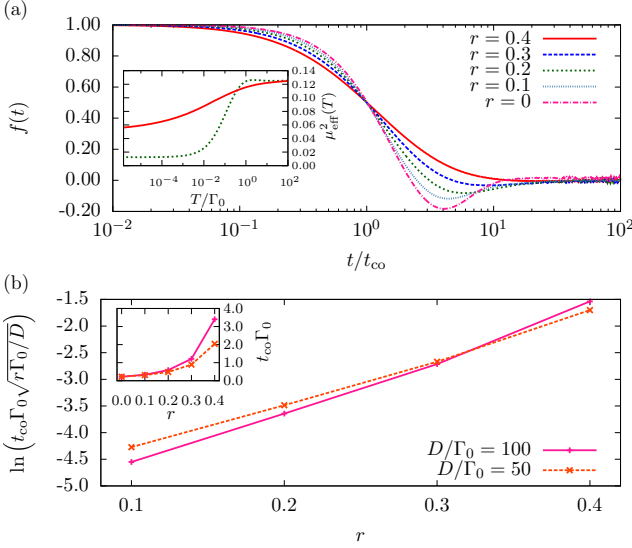


FIG. 5. (Color online) (a) The universal $f(t)$ versus t/t_{co} for different exponents $r = 0, 0.1, 0.2, 0.3, 0.4$. In the inset of (a) the temperature-dependent equilibrium effective local moment of the impurity spin $\mu_{eff}^2(T)$ is depicted for H_f , $D/\Gamma_0 = 100$, and $r = 0.2, 0.4$. (b) $\ln(t_{co}\Gamma_0\sqrt{r\Gamma_0/D})$ vs r while inset shows $t_{co}(r)\Gamma_0$.

find universality in $f_r(t/t_{co})$ for fixed r ; the different universal functions for different r are depicted in Fig. 5(a). With decreasing r the universal curve shows a dip at short times after which it increases again to the long-time value. This correlates to a small peak structure in the effective local moment $\mu_{eff}^2(T)$ for small r as depicted in the inset of Fig. 5(a).

In order to extract the r dependence of the universality time scale, we plot $\ln(t_{co}\Gamma_0\sqrt{r\Gamma_0/D})$ vs r in Fig. 5(b) where the inset of the panel shows the bare time scale t_{co} . Scaling t_{co} with \sqrt{r} for $r \geq 0.1$, we found an exponential dependency of the time scale t_{co} on r ,

$$t_{co} \propto \frac{e^{m(D)r}}{\sqrt{r}} \sqrt{\frac{D}{\Gamma_0}} \quad (13)$$

with a bandwidth-dependent exponent $m(D)$ by fitting the numerically obtained data to (13). Note, however, that the phenomenological estimate (13) for the time scale does not interpolate to $r \rightarrow 0$ and, therefore, is only valid for $0.1 \leq r < 1/2$.

When the charge-fluctuation scale Γ_0 approaches the band width D , the non equilibrium dynamics is dominated by local high-energy oscillations and, therefore, is non-universal as already indicated above. We present the time evolution of the double occupancy for the case $D/\Gamma_0 = 1$ in Fig. 6. We have plotted $\langle D(t) \rangle$ versus $t\sqrt{U_f D}$ for $U_f/\Gamma_0 = 0.5, 1, 2, 3, 4$ to reveal the quadratic decrease $\langle D(t) \rangle = 0.25(1 - \alpha(t/t_{short})^2)$ where the short-time scale $1/t_{short}^2 \propto U_f$. It steams from a linear contribution of $Un_{\uparrow}n_{\downarrow}$ in a perturbative expansion of the time-dependent density operator after the interaction quench.

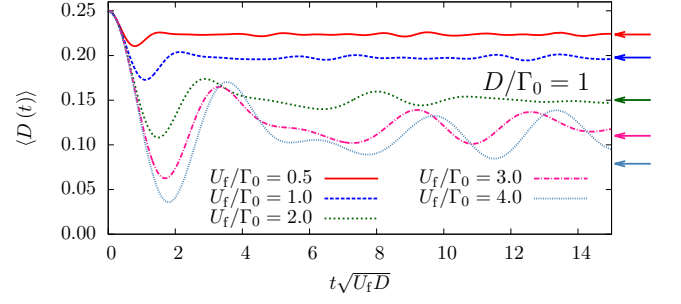


FIG. 6. (Color online) $\langle D(t) \rangle$ for quenches within the SC phase for hybridizations of the order of the band width $D/\Gamma_0 = 1$ and different Coulomb repulsions $U_f/\Gamma_0 = 0.5, 1, 2, 3, 4 < U_c/\Gamma_0 \simeq 4.426$ at temperature $T/\Gamma_0 \sim 10^{-6}$. As a guide to the eye the equilibrium expectation values after the quench are marked by the arrows at the right side of the graph.

For $U_f/\Gamma_0 = 2$ the local single-particle excitation energies E_d and $E_d + U$ approach the band edges; for $U_f/\Gamma_0 = 3, 4$ they exceed the band edges. Then, these states are only weakly coupled to the continuum with a finite energy gap preventing thermalization.

The short-time dynamics of $\langle D(t) \rangle$ depicted in Fig. 6 suggests a damped oscillation with a frequency that is only weakly U_f dependent. Asymptotically, the double occupancy only thermalizes to the equilibrium value obtained directly with H_f for smaller values of U_f . With increasing U_f , $\langle D(\infty) \rangle$ is decreasing and, therefore, the oscillation amplitude must increase.

In order to gain some understanding on the origin of these short-time oscillations we consider the limit of a vanishing band width at a constant hybridization $\pi V_0^2 = \int d\varepsilon \Gamma(\varepsilon) = \text{const}$. In this case we are left with a purely local problem described by the r -independent Hamiltonian H_0 of the first Wilson shell [3] whose eigenenergies are analytically known [3]. In this limit, there would be no damping, and we find a perfect oscillatory solution for $\langle D(t) \rangle$ whose frequency is determined by the difference of eigenenergies. A careful analysis of the local dynamics reveals that the oscillation of $\langle D(t) \rangle$ can be traced back to an admixture of two singlet states in the charge sector $Q = 0$ (the quantum number Q measures the deviation from half filling [3]) in the ground-state wave function. The difference of the eigenenergies of those states labeled by $r = 1$ and $r = 2$ in Table I of Ref. [3] coincide with the oscillation frequency extracted from $\langle D(t) \rangle$.

When we release the constraint of a vanishing band width, additional DOFs of the Wilson chain need to be included in the analysis. Adding a single additional Wilson chain link, i.e. $H_0 \rightarrow H_1$, immediately causes a more complex response due to the splitting of these eigenfrequencies. Since $V_0/D \approx 1$ for $\Gamma_0/D = 1$, the energy splitting of the eigenenergies due to an increasing Wilson chain length must be smaller than D and, therefore, V_0 and U . Hence the short-time dynamics on time scales

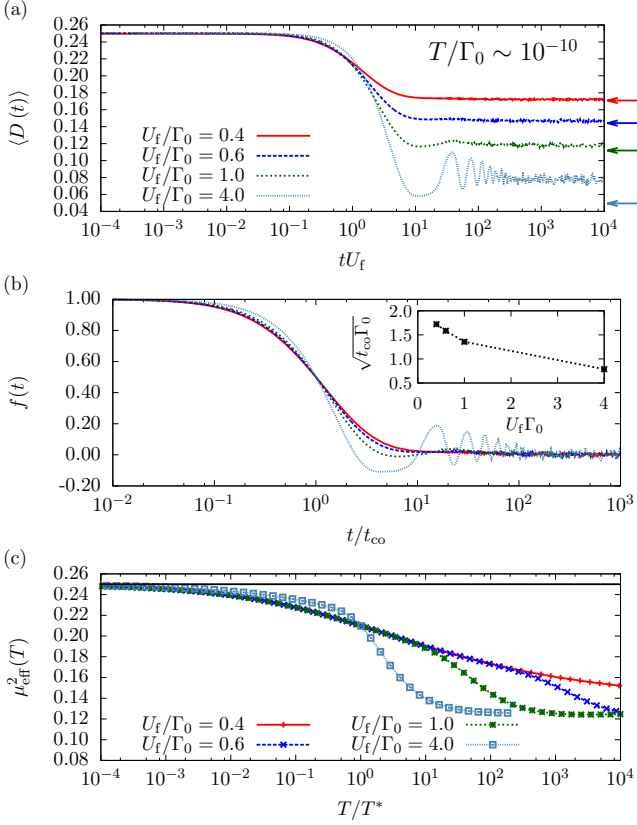


FIG. 7. (Color online) $\langle D(t) \rangle$ for quenches from the SC FP ($U_i = 0$) into the LM phase for different Coulomb repulsions $U_c/\Gamma_0 \approx 0.3392 < U_f/\Gamma_0 = 0.4, 0.6, 1, 4$ for a wide band $D/\Gamma_0 = 100$. (a) $\langle D(t) \rangle$ versus tU_f at $T/\Gamma_0 \sim 10^{-10}$. As a guide to the eye the equilibrium expectation values after the quench are marked by the arrows at the right side of the graph. (b) Same data rescaled with Eq. (11) to $f(t)$ versus t/t_{co} . In the inset the dependence of t_{co} by U_f . (c) The corresponding effective local moment of the impurity spin $\mu_{eff}^2(T)$ for the parameters U_f used in (a).

much shorter than tU_f is dominated by energy differences coming from a slightly modified local dynamics. This is the origin of the pronounced minimum observed in $\langle D(t) \rangle$ in Fig. 6.

When the local excitation energies E_d and $E_d + U$ are lying inside the band continuum, i.e. $|E_d|, |E_d + U| \leq D$, we observe thermalization. Once these local energies exceed the band continuum, bound states are formed outside of the band which contribute to the expansion of the initial ground state but cannot provide a relaxation channel. Even though we remain in the SC phase, $\langle D(t) \rangle$ cannot thermalize and remain oscillatory. This is the case for $U_f/\Gamma_0 = 3, 4$.

2. Quenches across the QCP

In this section we investigate interaction quenches across the QCP from the SC into the LM phase. Ini-

tially the system is prepared in the SC FP at $t = 0$ by setting $U_i = \epsilon_i = 0$.

For Coulomb repulsions $U_c < U_f$ the equilibrium properties of H_f governing the real-time dynamics belong to the LM phase. The LM FP can be described by an effective local moment comprising a linear combination of the impurity spin and the conduction electron bath spins in addition to a decoupled remaining free effective conduction electron band. Therefore, a finite equilibrium double occupancy $\langle D \rangle_{eq}$ remains present even in the LM phase.

Similarly to the Kondo temperature T_K that determines the low-energy crossover to the SC fixed point, the characteristic temperature T^* governs the crossover to the LM FP for $U > U_c$. We have defined T^* as $\mu_{eff}^2(T^*) = 0.21$ and plotted $\mu_{eff}^2(T)$ versus T/T^* to illustrate the universality in Fig. 7(b). We note that $T^* \propto (U - U_c)^{\nu(r)}$ with $\nu(r) = 4.3$ for $r = 0.4$, and T^* vanishes at $U = U_c$.

In Fig. 7(a) we present $\langle D(t) \rangle$ for quenches over the QCP with $U_c/\Gamma_0 \approx 0.3392 < U_f/\Gamma_0 = 0.4, 0.6, 1, 4$ for a wide band $D/\Gamma_0 = 100$ and temperature $T/\Gamma_0 \sim 10^{-10}$. The data obtained at a temperature $T/\Gamma_0 \sim 10^{-6}$ remains indistinguishable from the results depicted in Fig. 7(a) and, therefore, $T \rightarrow 0$. Even though $T > T^*$ for the lowest U_f value, the real-time dynamics remains temperature-independent and is only governed by the overlap of the initial ground state with the eigenstates of the final Hamiltonian.

We have plotted the data as function of the dimensionless time tU_f to reveal the time scale of the short-time dynamics. For quenches within the SC phase, we have demonstrated that the characteristic time scale is independent of U_f . For quenches across the QCP into the LM phase, we find that the time scale is proportional to $1/U_f$. The real-time dynamics is dominated by the local dynamics since part of the impurity DOFs decouple from the rest of the conduction band to participate in the local moment formation.

The characteristic energy scale T^* extracted from the universality of $\mu_{eff}^2(T)$ in the LM phase depicted in Fig. 7(b) increases with increasing distance $U - U_c$ to the QCP. The length scale $\xi^* = v_F/T^*$ used as an estimate for the spatial extension of the local moment decreases with increasing U . The decoupled spin DOFs become more localized and, consequently, the thermalization is increasingly suppressed with increasing U_f .

For $U_f/\Gamma_0 = 4$, we observe a decaying oscillatory behavior driven by a frequency proportional to U_f with a strong deviation between the long-time steady-state and the thermal equilibrium. For the smallest two interactions, $U_f/\Gamma_0 = 0.4, 0.6$, however, we found a steady-state value that is very close to the thermodynamic result and, therefore, can be considered as evidence for thermalization.

Although the equilibrium expectation value $\langle D \rangle_{eq}$ is continuously reduced with increasing U even across the QCP U_c , Fig. 7(a) demonstrates nicely the qualitatively different response for quenches across the QCP versus the

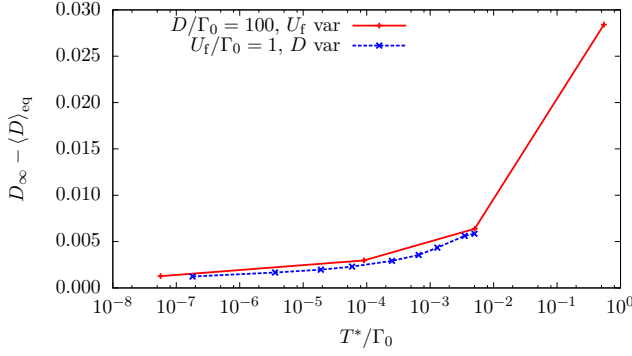


FIG. 8. (Color online) Difference between the long-time steady-state value D_∞ and the thermodynamic equilibrium value $\langle D \rangle_{\text{eq}}$ as function of T^* either for fixed D/Γ_0 and a variation of U_f (red curve) or a fixed U_f/Γ_0 and a variation of D (blue curve).

previously investigated dynamics within the SC phase in Sec. IIIB 1. While the characteristic time scale only depends on Γ_0 for quenches within the SC phase and shows universal behavior as long as all local excitations remain in the bath continuum, the real-time dynamics across the QCP is governed by $1/U_f$.

In order to illustrate the connection between the spatial extension of the local moment and thermalization we calculated the difference between the steady-state value D_∞ defined as

$$D_\infty = \lim_{T \rightarrow \infty} \frac{1}{T} \int_0^T dt \langle D(t) \rangle \quad (14)$$

and the thermal equilibrium value $\langle D \rangle_{\text{eq}}$ obtained for H_f . The results are depicted versus T^*/Γ_0 in Fig. 8 using the data of Fig. 7. Close to the QCP, the deviation is less the 3% given by the typical discretization error of the TD-NRG. For increasing U_f the deviation increases, supporting the picture of an increasingly localized free moment, leading to an increasing non decaying fraction of the local double occupancy.

We also have supplemented data for fixed $U_f/\Gamma_0 = 1$ but a variation of D as crosses connected with a blue line (color online) in Fig. 8. Interestingly, the deviation $\Delta D = D_\infty - \langle D \rangle_{\text{eq}}$ follows the same trend, and agrees within the numerical error with the data for fixed D/Γ_0 when approaching the QCP.

The deviation ΔD systematically increases with increasing T^* . Once T^* becomes large, the physics changes to an effectively decoupled free moment that is strongly localized and therefore prevents thermalization of the local expectation values.

Our results are in contrast to the results of Fig. 3 in Ref. [16] where these types of quenches were examined by a time-dependent Gutzwiller approach. Therein it was reported that the double occupancy $\langle D(t) \rangle$ strongly oscillates and never reaches a steady-state value at long times.

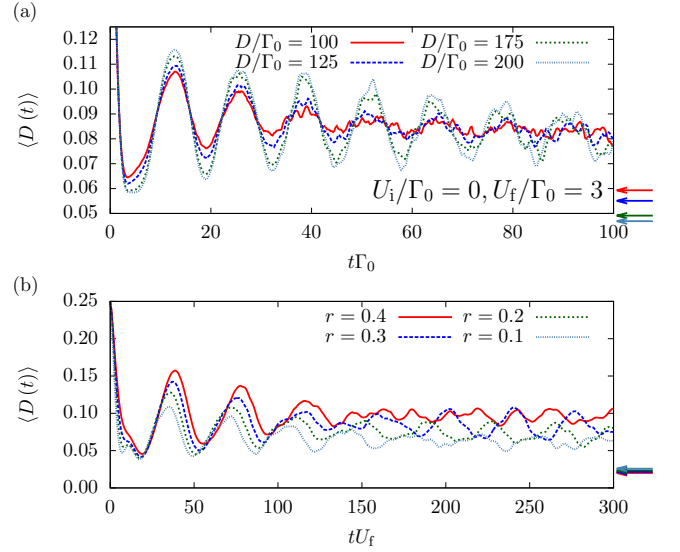


FIG. 9. (Color online) $\langle D(t) \rangle$ for interaction quenches from the SC FP into the LM phase. (a) $\langle D(t) \rangle$ versus $t\Gamma_0$ for different band widths $D/\Gamma_0 = 100, 125, 175, 200$, $r = 0.4$, and a fixed $U_f/\Gamma_0 = 3 > U_c$. (b) $\langle D(t) \rangle$ versus tU_f for different exponents r , fixed $D/\Gamma_0 = 100$, and adjusted Coulomb repulsion $U_f(r = 0.4)/\Gamma_0 = 14.72$, $U_f(r = 0.3)/\Gamma_0 = 17.73$, $U_f(r = 0.2)/\Gamma_0 = 21.06$, and $U_f(r = 0.1)/\Gamma_0 = 24.79$ such that $\langle D(U, r) \rangle_{\text{eq}} \approx 0.02$. Equilibrium expectation values after the quench are marked by the arrows at the right side of the graphs.

The reason for this disagreement is the nature of the Gutzwiller state whose dynamics has been traced via a time-dependent Gutzwiller equation [16]. This ansatz wave function is not able to properly represent the LM phase: $\langle D \rangle_{\text{eq}}$ vanishes for $U > U_c$ and is taken as an indicator for the QPT while an equilibrium NRG calculation [6] has proven the continuity of $\langle D \rangle_{\text{eq}}$ across U_c ; see also Fig. 2. While the NRG correctly contains the spatially extended nature of the decoupled local moment, the Gutzwiller state restricts the free moment to the local impurity site. Therefore, the time-dependent Gutzwiller approach is restricted to the strong-coupling regime.

In Fig. 9(a) we examine the effect of the bandwidth D on the real-time dynamics using four different values $D/\Gamma_0 = 100, 125, 175, 200$ for a constant ratio $U_f/\Gamma_0 = 3$. For this series, $U_c(D/\Gamma_0 = 100)/\Gamma_0 = 0.3358$ has the largest value and decreases further with increasing band width D . So U_f exceeds U_c almost by one decade even for the largest U_c .

Therefore, we quench deeper into the LM phase, indicated by a decreasing equilibrium double occupancy $\langle D \rangle_{\text{eq}}$; see arrows at right side of the graph. With increasing band width D , the amplitude of the damped oscillations are increased while the frequency is only proportional to U_f .

In Fig. 9(b) we vary the bath exponent r for a fixed ratio $D/\Gamma_0 = 100$ and choose U_f such that the equilibrium expectation value $\langle D(U_f) \rangle_{\text{eq}} \approx 0.02$ remains nearly

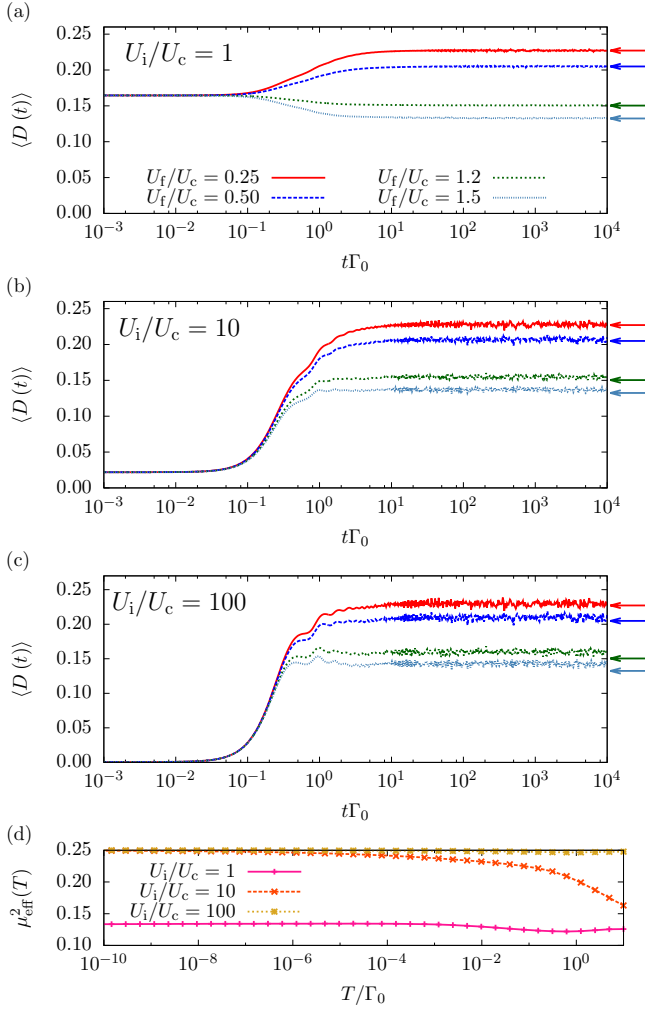


FIG. 10. (Color online) $\langle D(t) \rangle$ vs $t\Gamma_0$ for four different values of U_f . For quenches within the LM phase we set $U_f/U_c = 1.2, 1.5$ and for quenches across the QCP we choose $U_f/U_c = 0.25, 0.5$. All data have been obtained for $D/\Gamma_0 = 10$. In the different panels (a)–(c) different initial Coulomb repulsions have been used: (a) $U_i/\Gamma_0 \approx U_c/\Gamma_0 = 1.5088$, (b) $U_i/U_c = 10$, and (c) $U_i/U_c = 100$. (d) Effective moment $\mu_{\text{eff}}^2(T)$ for the different U_i .

constant for all r as indicated by the arrows on the right side. $\langle D(t) \rangle$ is plotted versus tU_f to remove the leading order frequency dependency of the oscillations for different Coulomb interactions U_f . The remaining small frequency shift with increasing r is related to the different ratios U_f/Γ_f : the larger r , the larger the ratio Γ_f/U_f and corrections of the order $\sqrt{1 + 2\Gamma_f D/(\pi U^2)}$ need to be taken into account stemming from the energy difference of eigenstates of the first Wilson shell as previously discussed in the context of Fig. 6.

3. Quenches from the LM phase

In a reverse type of quench the initial U_i , exceeding the critical U_c , is reduced to values U_f that are either larger than U_c , such that the system remains in the LM phase, or $U_f < U_c$, for quenching across the QCP into the symmetric SC phase. The initial value of $\langle D(t=0) \rangle$ depends on the distance $U_i - U_c$ and reaches $\langle D(t=0) \rangle \rightarrow 0$ for $U_i \rightarrow \infty$. Since we always maintain ph symmetry, $2\varepsilon_d(t) + U(t) = 0$ holds at any time.

In order to investigate the dependency of U_i , we calculate the real-time dynamics for three different values $U_i \approx U_c$, $U_i/U_c = 10$, and $U_i/U_c = 100$. The results are depicted in Figs. 10(a)–10(c). Each graph shows $\langle D(t) \rangle$ for a fixed U_i and a series of four values of U_f : For quenches within the LM phase, we use $U_f/U_c = 1.2, 1.5$ while for quenches across the QCP into the SC phase we choose $U_f/U_c = 0.25, 0.5$.

The initial value $\langle D(t=0) \rangle$ decreases with increasing value U_i . Starting with $U_i/U_c = 1$, we observe an increase of D_∞ for $U_f < U_c$ and a decrease for $U_f > U_c$ as expected. Furthermore, $D_\infty \approx \langle D \rangle_{\text{eq}}(U_f)$ as indicated by the arrows on the right side of Fig. 10(a) which we interpret as indication for thermalization.

For Fig. 10(b), we have prepared the system with $U_i/U_c = 10$, and quench to the same four final values of U_f as in Fig. 10(a). Again, the initial short-time dynamics is U_f -independent, starting from a much smaller initial value. The saturation is almost reached at $t\Gamma_0 \approx 1$. However, we observe a slight deviation from the thermal equilibrium. Those deviations remain negligibly small for quenches from the LM to the SC phase but become visible for quenches within the LM phase: the deviations are of the order of 7%. For the last value $U_i/U_c = 100$, starting deep in the LM phase with a completely suppressed initial double occupancy, the short-time dynamics is again U_f -independent and the steady-state value is approached very fast, governed by the time scale of $1/\Gamma_0$. However, the deviation from the thermal equilibrium is much more pronounced and reaches about 15% for $U_f/U_c = 1.5$.

4. Quenches with particle-hole asymmetry

So far we have restricted ourselves to particle-hole (ph) symmetry, namely $U(t) = -2\varepsilon_d(t)$. Now we investigate the influence of ph-symmetry breaking on the real-time dynamics. We recall that the asymmetric strong-coupling (ASC) fixed point [6–8, 21, 43] differs from the SC FP by a complete screening of the impurity spin independently of r . Furthermore, the equilibrium double occupancy $\langle D \rangle_{\text{eq}}$ in the ASC FP depends on the asymmetry $|U - 2\varepsilon_d|$ and the band exponent r : With increasing asymmetry or increasing r the equilibrium double occupancy ($\langle D \rangle_{\text{eq}} = 1/4$ for ph symmetry) increases.

In Fig. 11(a) $\langle D(t) \rangle$ is shown for two different initial conditions: The dashed lines describes the time evolution starting from the particle-hole asymmetric phase (ASC)

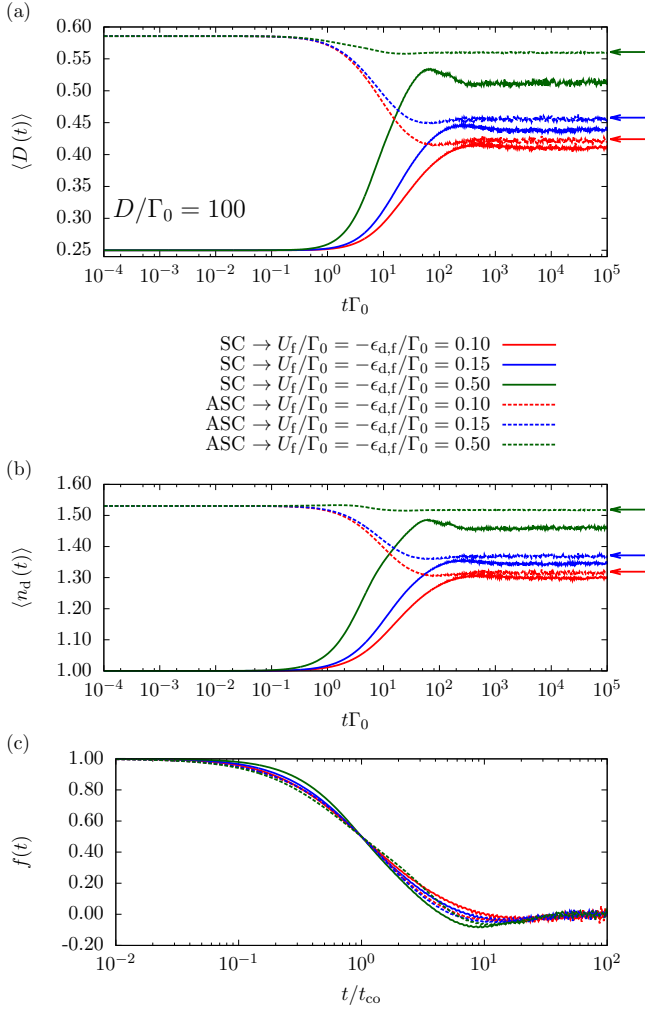


FIG. 11. (Color online) (a) $\langle D(t) \rangle$ vs $t\Gamma_0$ for particle-hole asymmetry. We quench either from the SC FP ($U_i = \epsilon_{d,i} = 0$) or the ASC FP ($U_i = 0, \epsilon_{d,i}/\Gamma_0 = -0.1$) into or rather within the ASC phase. All data have been obtained for $D/\Gamma_0 = 100$ and $r = 0.4$. (b) Change of the local occupancy $\langle n_d(t) \rangle$ vs time for the same parameter as in (a). In (c) the data of (a) rescaled via Eq. (11) to $f(t)$ versus t/t_{c0} with the crossover time scale t_{c0} .

using the parameters $U_i = 0, \epsilon_{d,i}/\Gamma_0 = -0.1$ while the solid lines depict the time evolution starting from the particle-hole symmetric point $U_i = \epsilon_{d,i} = 0$ as initial condition. The different colors distinguish the different values of the final Hamiltonian. Since the filling is also changing with time, we augment the data by showing the change of the impurity filling $\langle n_d(t) \rangle$ in Fig. 11(b) for the same parameter.

Although a steady state is always found, only quenches starting from a particle-hole symmetry broken state thermalize as indicated by the arrows of equilibrium double occupancy value on the right-hand side of Figs. 11(a) and 11(b). The deviation of the steady-state value from the thermal value when changing the degree of particle-hole asymmetry is a shortcoming of the TD-NRG [14, 32, 44]

and has recently been investigated in great detail [15].

We have applied the same scaling procedure to the data of Fig. 11(a) as in Fig. 4 and have plotted the results in Fig. 11(c). Qualitatively a similar behavior is found. However, universality is lost, and the shape of the dimensionless function depends on the degree of particle-hole asymmetry.

C. Hybridization quenches

Up to now, we have investigated interaction quenches. In this section, we focus on a second type of quench, the hybridization quenches. They are defined by switching the hybridization strength $\Gamma_0 \rightarrow \Gamma(t) = \Theta(-t)\Gamma_i + \Theta(t)\Gamma_f$ between the initial value Γ_i and the final value Γ_f at time $t = 0$. In contrast to the previous sections, we keep here the Coulomb repulsion $U_i/D = U_f/D = \text{const}$ and finite at all times and restrict ourselves to particle-hole symmetry. In order to have a well-defined, unique reference point, we choose $\Gamma_i = 0$ implying that the system is initially prepared in the LM FP whose ground state is U -independent with a double occupancy $\langle D(t=0) \rangle = 0$ for all parameters.

Since we change Γ_0 , we use the band width D as unit of energy in this section. The terms short, intermediate, and long times will correspond to $tD \ll 1$, $tD \sim 1$, and $tD \gg 1$.

As discussed in Sec. II C, H_f has two different low-energy FPs depending on Γ_f . For $\Gamma_f < \Gamma_c$, the LM FP is reached at low temperature in equilibrium, while for $\Gamma_f > \Gamma_c$, the system is described by the symmetric SC FP. We have checked that the equilibrium FP has been reached for all parameters such that the real-time dynamics results correspond to $T \rightarrow 0$.

1. Quenches within the LM phase

We start with quenches within the LM phase, i.e. $\Gamma_f < \Gamma_c$, and present data in the wide-band limit by setting $D/U = 100 = \text{constant}$. The results for the time-dependent double occupancy $\langle D(t) \rangle$ are depicted for the short-time dynamics in Fig. 12(a) and the long-time asymptotic in Fig. 12(b) for $\Gamma_f/D = 0.002, 0.004, 0.008, 0.012, 0.016 < \Gamma_c/D \approx 0.019$.

The double occupancy $\langle D(t) \rangle$ rises quickly from its initial value and exhibits a peak at intermediate times before it falls off towards a steady-state value. With increasing hybridization Γ_f the peak height raises and is more pronounced. Plotting all data versus the dimensionless time $\tau = t\sqrt{\Gamma_f D}$ reveals that the short-time dynamics is U -independent and only driven by the final hybridization strength Γ_f .

Although a steady state is reached, the difference to the thermodynamic equilibrium value – indicated by the arrows in Fig. 12(b) – is significant and increases with increasing Γ_f . This indicates that the real-time dynamics

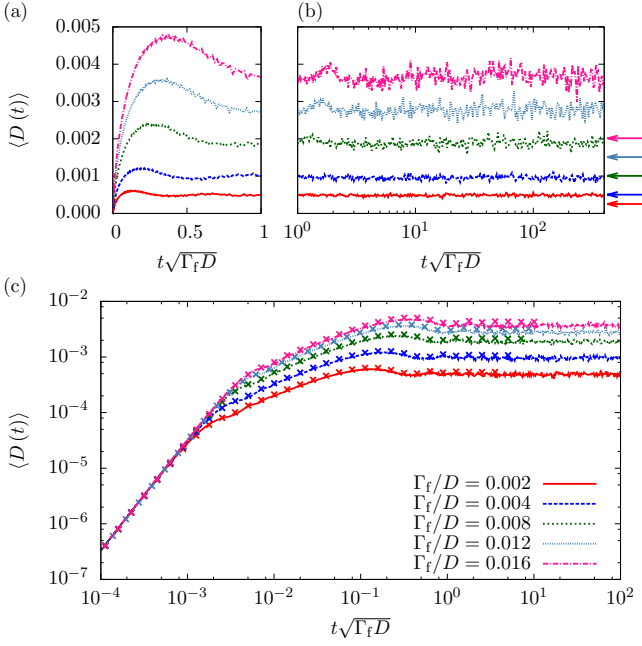


FIG. 12. (Color online) Quenches from the LM FP at time $t = 0$ within the LM phase. The hybridization is $\Gamma_f/D = 0.002, 0.004, 0.008, 0.012, 0.016 < \Gamma_c/D \simeq 0.019$ with a constant Coulomb repulsion $U/D = U_i/D = U_f/D = 0.01$ and $r = 0.4$. $\langle D(t) \rangle$ (a) for short times, (b) for long times on log time scale. As a guide to the eye the equilibrium expectation values after the quench are marked by the arrows at the right side of (b). For all hybridizations Γ_f the system does not thermalize. (c) Same data as (a) and (b) on a logarithmic y scale. Additionally we added the result of the second-order perturbation theory [cf. Eq. (15)] represented by the crosses.

is not governed by the FP properties but from the overlap of the initial wave function with the excited states of H_f .

Deviations from the thermodynamic equilibrium could originate in limitations of the method due to the discretization of the conduction band continuum [14, 15, 32, 44]. The low-energy FP of H_f , however, is still given by the LM FP with a twofold-degenerate ground state so that the increase of the deviation with increasing Γ_f is explained. Varying Γ_f within the LM phase has a profound impact on the physics. With increasing Γ_f the system approaches Γ_c and, therefore, the characteristic energy scale T^* decreases. This implies that the effective spin moment decoupling from the rest of the system becomes more extended with increasing Γ_f and a larger fraction of the impurity DOFs hybridize with the conduction band leading to an continuous increase of $\langle D \rangle$. There are two states of finite range that form the effective moment decoupling from the rest of the chain. An admixture of those states to the initial ground state cannot relax further due to the decoupling of these states in the LM regime. Consequently, we observe a state-state differing significantly from the thermal state.

2. Analytic result for the short-time dynamics

In order to shed some more light onto the dynamics for hybridization quenches when $\Gamma_f < \Gamma_c$, we analytically calculate $\langle D(t) \rangle$ for the short-time dynamics. Knowing all eigenstates and eigenenergies for $\Gamma_0 = 0$, we expand the time-dependent density operator in powers of the hybridization, and evaluate $\langle D(t) \rangle$ exactly up to second order – see the Appendix for more details.

The short-time dynamics of the double occupancy is given by the analytic expression

$$\langle D(t) \rangle = \frac{\Gamma_f D}{\pi} t^2 + \frac{2\Gamma_f(1+r)}{\pi} \sum_{n=2}^{\infty} \frac{(-1)^{2n}}{(2n)!} \times \int_{-D}^0 \left| \frac{\epsilon}{D} \right|^r ((\epsilon - \epsilon_d - U)t)^{2n} d\epsilon \quad (15)$$

which is asymptotically exact for $t \rightarrow 0$. In leading order in t , $\langle D(t) \rangle$ increases quadratically in time with a U -independent prefactor $\Gamma_f D/\pi$ defining the squared characteristic time scale for the short-time dynamics. Our analytical result confirms the dimensionless time scale $\tau = t\sqrt{\Gamma_f D}$ used previously in Fig. 12 to reveal the universality in the short-time TD-NRG response. The U -dependent corrections enter the higher terms in t and account for a weak oscillation.

In order to illustrate the leading t^2 behavior in the short-time dynamics of the full TD-NRG calculations and their excellent agreement with the analytical result for the full continuum, we present the numerical results of Figs. 12(a) and 12(b) in a log-log plot as Fig. 12(c). We added the analytical results of Eq. (15) for selected times as crosses in the same color. Numerics and analytics coincide perfectly for short and intermediate times even up to $t\sqrt{\Gamma_f D} \approx 1$. The analytical result does not only describe the leading order $O(t^2)$ term correctly but also accounts for the deviation from the parabola starting at $t\sqrt{\Gamma_f D} \approx 10^{-3}$ and the long-time steady state. Of course the deviation between the analytic steady-state value and the TD-NRG results is stronger with increasing Γ_f as expected from the perturbative nature of the analytical approach.

3. Energy flow in the LM phase

Another interesting question arises as to whether the deviation $\Delta O = O_{\infty} - \langle O \rangle_{eq}$ of the long-time limit O_{∞} [45, 46],

$$\begin{aligned} O_{\infty} &= \lim_{T \rightarrow \infty} \frac{1}{T} \int_0^T dt \langle O(t) \rangle \\ &= \sum_m^N \sum_{\substack{r,s \\ E_r=E_s}}^{\text{trun}} O_{r,s}^m \rho_{s,r}^{\text{red}}(m) \end{aligned} \quad (16)$$

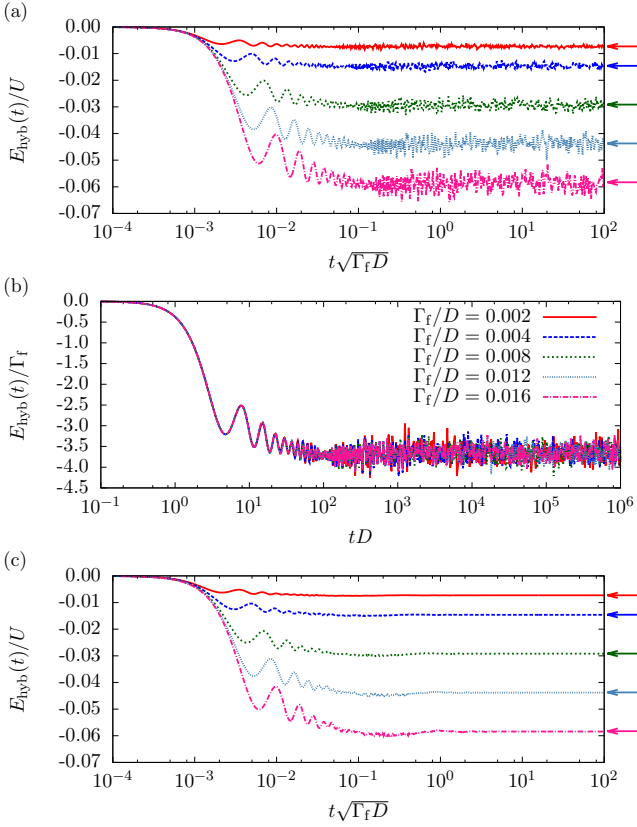


FIG. 13. (Color online) The hybridization energy $E_{\text{hyb}}(t)$ vs time for hybridization quenches within the LM phase using a constant Coulomb repulsion $U_i/D = U_f/D = U/D = 0.01$ and various hybridization strengths $\Gamma_f/U = 0.2, 0.4, 0.8, 1.2, 1.6 < \Gamma_c/U \simeq 1.9$. (a) $E_{\text{hyb}}(t)/U$ vs the dimensionless time $\tau = t\sqrt{\Gamma_f D}$ characterizing the dynamics of the double occupancy, and (b) $E_{\text{hyb}}(t)/\Gamma_f$ vs tD . (c) Same quenches as (a) but calculated with an additional TD-NRG broadening $\alpha = 0.4$.

from its thermal expectation value $\langle O \rangle_{\text{eq}}$ with respect to the final Hamiltonian is operator-dependent, and therefore, different physical properties show different thermalization behavior for the same quench. Furthermore, it has been conjectured that the choice of a Wilson chain might be not suitable for properly describing hybridization quenches [29] because the NRG chain might not be able to serve as a heat reservoir for larger changes in the hybridization energy. However, Wilson's NRG as well as the TD-NRG target only the local dynamics and corresponding bath expectation values do not have any physical meaning: A discretized finite bath, as used in any NRG calculation, has always only finite energy content while the thermodynamic bath provides a reservoir with infinitely large energy. Since a quantum state by itself can never thermalize when subject to the energy conserving dynamics defined by the Schrödinger equation, one needs to restrict such an investigation to quantum impurity expectation values. The deviation from a corresponding equilibrium NRG calculation using identical

discretization parameters serves as a criterion of how well the quantum impurity subsystem is able to thermalize.

Both questions can be addressed by investigating the local energy flow for quenches within the LM phase for the quench parameters presented in Fig. 12. For those parameters we have established already above that thermalization of the double occupancy $\langle D(t) \rangle$ is absent, and switching on the hybridization results in an overestimation of the double occupancy compared to the thermal equilibrium that increases with Γ_f . For particle-hole symmetry, $E_d n_d$ is discontinuous at $t = 0$, since work has been performed on the system, but afterwards $E_d n_d$ remains constant for $t > 0$. In addition, the contribution of $U \langle D(t) \rangle$ to the impurity energy is very small compared to $E_{\text{hyb}}(t) = \langle H_{\text{hyb}}(t) \rangle$. Therefore, the main energy flow of the impurity is governed by the hybridization energy $E_{\text{hyb}}(t)$ which is initially zero for $t \leq 0$. Note that the hybridization energy $E_{\text{hyb}}(t)$ involves in addition to the impurity operator only the local host degree of freedom on the first Wilson shell [3, 4] and, therefore, is a local operator as required for the TD-NRG [13, 14].

The results of $E_{\text{hyb}}(t)$ are depicted in Fig. 13: The arrows on the right side in Fig. 13(a) – depicting the thermal expectation value of the hybridization energy – indicate clearly that $E_{\text{hyb}}(t)$ is approaching its thermal equilibrium in the long-time limit, even though the system remains in the LM regime and $\langle D(t) \rangle$ does not equilibrate. $E_{\text{hyb}}(t)$ has been measured in units of the constant U and plotted versus $\tau = t\sqrt{\Gamma_f D}$. Clearly the dynamics is not governed by the characteristic time scale of the double occupancy.

Since the hybridization energy is proportional to Γ_f ,

$$\sum_{k\sigma} V_k \langle d_{\sigma}^{\dagger} c_{k\sigma} \rangle \propto \Gamma_f, \quad (17)$$

we have divided out the leading order prefactor of E_{hyb} , Γ_f , and have plotted E_{hyb}/Γ_f vs tD in Fig. 13(b). Surprisingly, the short-time dynamics of E_{hyb}/Γ_f appears to be universal and is governed by the band width D while the overall magnitude of E_{hyb} is determined by Γ_f for a finite $r = 0.4$. While for $r = 0$ $E_{\text{hyb}}/\Gamma_f \propto \ln(D/\Gamma_f)$ in equilibrium as it can be shown by a simple analytic calculation, this is not the case for $r > 0$: The larger r the less E_{hyb}/Γ_f depends on the ratio D/Γ_f for the wide-band limit. Since the hybridization energy approaches its steady-state value very fast, apparently this expectation value is not influenced by the buildup of low-energy correlations characterizing the LM FP.

On the first side this surprising thermalization of $E_{\text{hyb}}(t)$ seems to contradict the increasing deviation $\Delta D = D_{\infty} - \langle D \rangle_{\text{eq}}$ within the LM phase. The physical content of the two operators, however, is different. The impurity DOFs provide a major contribution to the effective moment formation which decouples from the rest of the system in the LM phase, while E_{hyb} probes the coupling to the full bath continuum. The number of bath DOFs contributing to the local moment formations are of measure zero in the integration over all k states so that

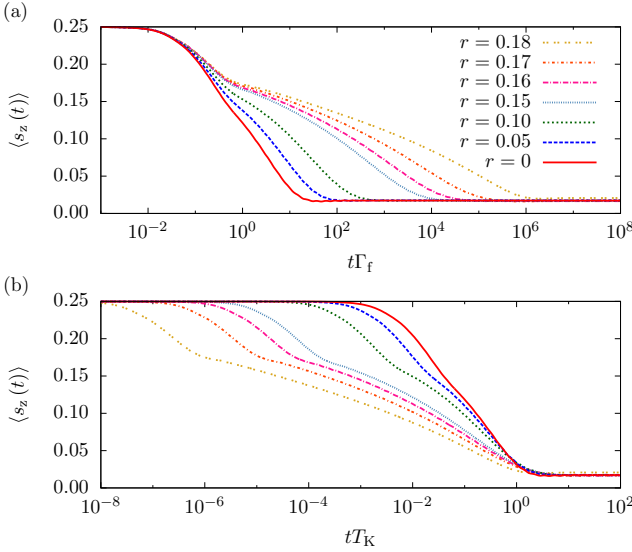


FIG. 14. (Color online) (a) Impurity magnetization $\langle s_z(t) \rangle$ vs (a) $t\Gamma_f$ and (b) vs tT_K for a fixed $U/\Gamma_f = 6$ and different bath exponents r . We quench $\epsilon_{d,i}/2\Gamma_f = H_i/\Gamma_f = 1 \rightarrow \epsilon_{d,f}/U_f = -1/2$, $H_f = 0$ and switch on the hybridization Γ_f from $\Gamma_i = 0$ at $T/\Gamma_f = 7 \cdot 10^{-7}$. The NRG parameters: $\Lambda = 1.6$, $N_S = 1500$, and $\alpha = 1$.

the main error in $E_{\text{hyb}}(t)$ can be traced back to TD-NRG discretization errors. Furthermore, the real-time dynamics of E_{hyb} is an ultrafast process governed by the bandwidth as shown in Fig. 13 and has approached its steady-state value on a time scale where long-time correlations have not had a chance to develop.

Our findings indicate that the magnitude ΔO strongly depends on the operator \hat{O} and the details of matrix elements $O_{r,s}^m$ selecting the states contributing to the long-time limit as well as defining the oscillation frequency distribution governing the real-time dynamics via Eq. (7).

4. Real-time dynamics of the impurity magnetization

By switching on an initial local magnetic field $H_i = \Gamma_f > 0$, we break the spin symmetry and induce a spin polarization in the initially decoupled impurity of $\langle s_z \rangle = 0.25$ independent of r , where $\langle s_z \rangle = \langle n_\uparrow - n_\downarrow \rangle / 2$.

$s_z(t) = \langle s_z(t) \rangle$ is shown in Fig. 14 after switching off the external magnetic field H for times $t > 0$. Note that we have used a broadening factor $\alpha = 1$ in Eq. (9) [13, 14] in this calculations to illustrate the difference to the z averaging. Results are shown for a fixed $U/\Gamma_f = 6$ but different r for particle-hole symmetry breaking initial conditions $\epsilon_{d,i}/2\Gamma_f = H_i/\Gamma_f = 1$ which imply $s_z(0) = 0.25$. We also have performed calculations for particle-hole symmetric initial conditions where the level position remains unaltered; i.e. $\epsilon_{d,i} = \epsilon_{d,f} = -U/2$ and consequently $s_z(0) = 0.5$ – not shown. Since $s_z(t)/2$ coincides perfectly with the data of Fig. 14(a), the time-dependency of the spin decay is controlled by the type of

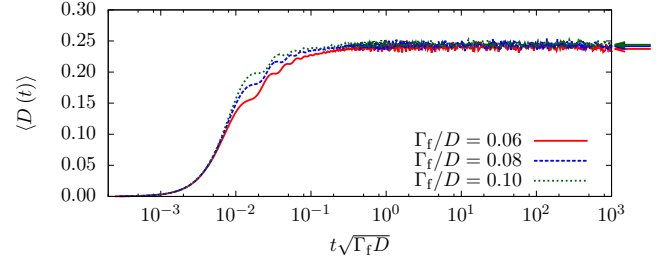


FIG. 15. (Color online) $\langle D(t) \rangle$ for hybridization quenches into the SC phase for a constant Coulomb repulsion $U/D = U_i/D = U_f/D = 0.01$. The hybridization strength Γ_f is set well above the critical value, $\Gamma_f/D = 0.06, 0.08, 0.1 > \Gamma_c/D \simeq 0.019$. Arrows at the right side mark the equilibrium expectation values after the quench.

quench and not by the initial amount of spin polarization.

Since $U > \Gamma_f$, the short-time spin decay is governed by the Schrieffer-Wolff exchange interaction [47]. After that fast initial spin decay which is independent of r , the spin relaxation slows down as the Kondo correlations start to build up [48]. The details of the spin decay strongly depend on the bath exponent r . This is not surprising since (i) the nature of the SC FP is different for each r and (ii) the critical coupling U_c decreases with increasing r . In Fig. 14(b), we have plotted the data as a function of the dimensionless time tT_K to reveal the long-time behavior. We have defined the Kondo temperature via the screening of the effective moment [12, 13], i.e. $\mu_{\text{eff}}^2(T_K) = r/8 + 0.07$, where we have factored in the r -dependent residual moment $\mu_{\text{eff}}^2(0) = r/8$. Similar to the findings in Fig. 3 of Ref. [13], T_K plays a role in determining different decay regimes in the real-time dynamics. For $tT_K < 1$ no universal behavior is found, but the potential universal behavior of $s_z(t)$ for very long times $tT_K \gg 1$ is obstructed by the finite resolution of the TD-NRG.

For $U < \Gamma_f$ but U close to U_c at larger $r > 0.3$ the above analysis does not hold. Here the spin decay is governed by the charge-fluctuation scale Γ_f and remains almost independent of T_K – not shown here. At short time scales controlled by high-energy excitation the existence of the pseudogap is less relevant and the dynamics is that of a weakly correlated system. A more in depth analysis of the complex spin dynamics in the pg-SIAM will be presented elsewhere.

5. Quenches across the QCP

Now we proceed with hybridization quenches across the QCP, from the initial LM FP with $\Gamma_i = 0$ into the symmetric SC phase with $\Gamma_c < \Gamma_f$.

The time-dependent double occupancy $\langle D(t) \rangle$ is depicted in Fig. 15 for $\Gamma_c/D < \Gamma_f/D = 0.06, 0.08, 0.1$. As for $\Gamma_f < \Gamma_c$, $\langle D(t) \rangle$ shows a fast rise with an universal time scale $1/\sqrt{\Gamma_f D}$ and saturates in the long-time limit at a stationary value which is very close to the thermo-

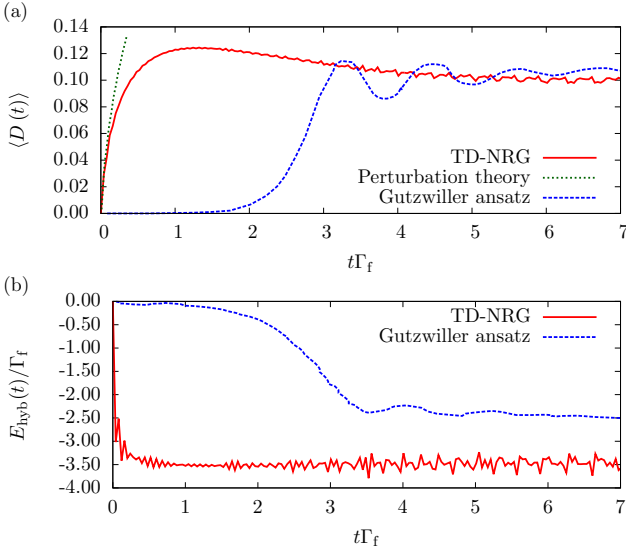


FIG. 16. (Color online) Comparison between the TD-NRG (solid line) and time-dependent Gutzwiller ansatz (dashed line) for a hybridization quench, i.e. $\Gamma_i = 0 \rightarrow \Gamma_f/D = 0.01$, and $r = 0.4$. The Gutzwiller data taken from Ref. [16] has been obtained for $U/\Gamma_f = 9$. (a) $\langle D(t) \rangle$ and (b) the time-dependent hybridization energy $E_{\text{hyb}}(t)$ for the NRG parameters $U_c/\Gamma_0 < U_i/\Gamma_f = U_f/\Gamma_f = 1.6$ and augmented with the Gutzwiller data. The NRG parameters have been chosen such that $D_{\infty}^{\text{TD-NRG}} \approx D_{\infty}^{\text{Gutz}}$ for a quantitative comparison.

dynamic limit. In contrary to the LM FP within the LM phase quench, the thermodynamic value $\langle D \rangle_{\text{eq}}$ deviates only very little from the free value of $\langle D \rangle_{\text{eq}} = 1/4$.

At intermediate times, $t\sqrt{\Gamma_f D} \approx 10^{-2}$ damped oscillations with an oscillation frequency $\propto U$ are superimposed onto the continuous rise of $\langle D(t) \rangle$ from the initial value $\langle D(0) \rangle = 0$ to the final steady-state value. For the real-time dynamics of the double occupancy the Kondo scale is irrelevant: The dynamics is governed by the short-time scale $1/\sqrt{\Gamma_f D}$, with superimposed oscillations depending on U .

6. Comparison with Gutzwiller results

In Sec. III A we have pointed out that the local equilibrium properties obtained by the accurate NRG approach deviate significantly from the approximate Gutzwiller approach. This discrepancy can be traced back to the physical content of the Gutzwiller ansatz wave function that focuses only on the local spin moment formation on the impurity site while the NRG ground state correctly accounts for the extended nature of the decoupling moment. Consequently, the local nature of Gutzwiller ansatz largely overestimates the critical U_c as already shown in Fig. 2.

A choice of identical model parameters always yields different local properties in the two different methods. In order to make a useful comparison between the ap-

proaches, we have chosen the NRG parameters such that the equilibrium double occupancies approximately agree between both approaches, i.e. $D_{\infty}^{\text{TD-NRG}} \approx D_{\infty}^{\text{Gutz}}$, as well as both approaches describe the same type of quench.

The Gutzwiller data are taken from Fig. 2 in Ref. [16] calculated for a hybridization quench in the wide-band limit with $U/\Gamma_f = 9$, and $r = 0.4$, where a hybridization quench from the initial LM phase into the SC phase across the QCP has been investigated.

While the equilibrium Gutzwiller approach predicts a screened local moment and hence describes the SC phase, these parameters would be located deeply in the LM phase in a NRG calculation. Therefore, we had to reduce U to $U/\Gamma_0 = 1.6 < U_c/D$ for the TD-NRG calculation to also maintain the NRG dynamics in the SC regime.

We compare the double occupancy $\langle D(t) \rangle$ from the TD-NRG and the Gutzwiller approach in Fig. 16(a). The Gutzwiller approach predicts a very long silent phase for $0 < t < 1/\Gamma_f$ after the quench, before $\langle D(t) \rangle$ steeply rises for $1 < t\Gamma_f$ and then approaches oscillatory the equilibrium value at long times. In contrast to these approximate results, the TD-NRG data perfectly agree with the analytical prediction of Eq. (15) for the short-time dynamics, predicting a fast quadratic raising of $\langle D(t) \rangle \approx t^2\Gamma_f D/\pi$ for short times before higher order terms cause a convergence to a finite value.

The origin of the long silent phase in the Gutzwiller approach is directly related to the slow increase of $|E_{\text{hyb}}|$ caused by the strong analytic restriction of the parameter space in the ansatz as can be seen from the equation of motion stated in the Supplemental Material of Ref. [16]. In the accurate TD-NRG, however, the energy flow away from the impurity is very fast and occurs on the time scale of the inverse band width.

7. Quenches for exponents $r > 1/2$

So far we restricted ourselves to exponents $0 < r < 1/2$ since a QCP can be found only for those values if $U > 0$. For $1/2 < r$ and $U > 0$, the system always approaches the LM FP for $T \rightarrow 0$ in equilibrium [6].

Let us briefly review the equilibrium properties of these regimes for varying the bath exponent r and a fixed $D/\Gamma_0 = 100$ depicted in Fig. 17. The effective local moment $\mu_{\text{eff}}^2(T)$ is plotted versus T in the strongly correlated regime $\Gamma_0/U = 0.1$ in Fig. 17(a) and in the weakly correlated regime $\Gamma_0/U = 10$ in Fig. 17(b) for $r = 0, 0.2, \dots, 1.2$. For $r = 0$ the system always approaches the SC FP with $\mu_{\text{eff}}^2(0) = \lim_{T \rightarrow 0} \mu_{\text{eff}}^2(T) = 0$ while for $0.2 \leq r < 1/2$, the symmetric SC FP with $\mu_{\text{eff}}^2(0) = r/8$ for $\Gamma_0/U = 10$, and the LM FP $\mu_{\text{eff}}^2(0) = 1/4$ for $\Gamma_0/U = 0.1$ is reached. For $1/2 < r$, the system always flows to the LM FP, and the crossover scale T^* is increasing with increasing r .

The corresponding equilibrium double occupancy $\langle D \rangle_{\text{eq}}$ versus r is shown in Fig. 17(c) for $T \rightarrow 0$. In the weakly correlated regime $\Gamma_0/U = 10$ the double oc-

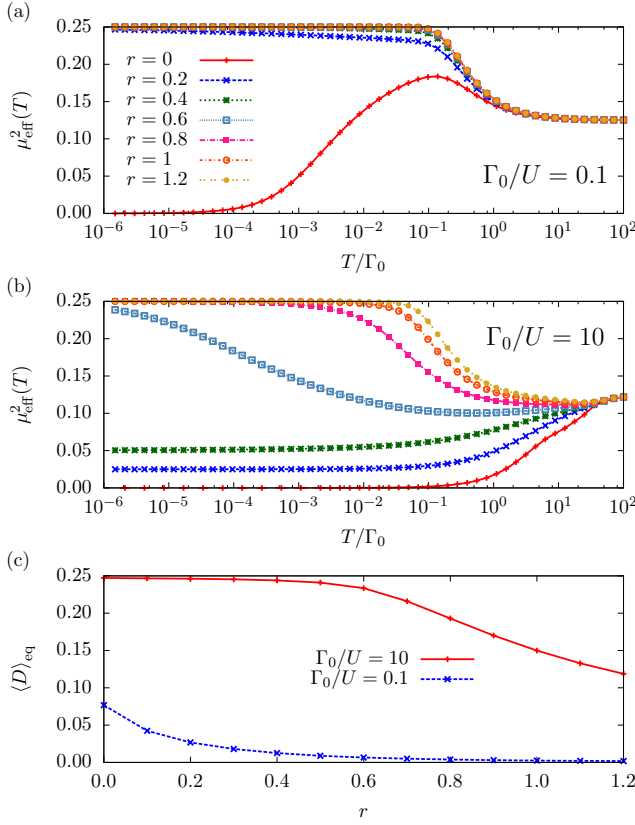


FIG. 17. (Color online) Equilibrium properties of the pg-SIAM in dependence of the bath exponent r and fixed $D/\Gamma_0 = 100$. (a) $\mu_{\text{eff}}^2(T)$ in a strongly correlated regime $\Gamma_0/U = 0.1$, and (b) in a weakly correlated regime $\Gamma_0/U = 10$. (c) The equilibrium double occupancy $\langle D \rangle_{\text{eq}}$ for both regimes for $T \rightarrow 0$.

cupancy $\langle D \rangle_{\text{eq}}$ remains close to the uncorrelated value of 0.25 and only weakly dependent on r for $0 < r < 1/2$. The slow decrease of $\langle D \rangle_{\text{eq}}$ is related to a reduced screening of the impurity with increasing r ; cf. increasing residual local moment in Fig. 17(b). For $1/2 < r$ the double occupancy $\langle D \rangle_{\text{eq}}$ declines much faster with increasing r since the system approaches the LM FP for $T \rightarrow 0$. For the strongly correlated regime $\Gamma_0/U = 0.1$, the double occupancy $\langle D \rangle_{\text{eq}}$ is already strongly suppressed for small r .

Now we present our results for hybridization quenches as a function of r for fixed $D/\Gamma_i = D/\Gamma_f = 100$ and fixed $\epsilon_d = -U/2$. The TD-NRG results for the double occupancy $\langle D(t) \rangle$ are depicted for two values for $\Gamma_f/U_f = 0.1, 10$ and $r = 0, 0.2, 0.4, 0.6, 0.8, 1.0, 1.2$ in Fig. 18.

With the exception of $r = 0$, Fig. 18(a) shows quenches within the LM phase. The double occupancy $\langle D(t) \rangle$ rises from its initial value towards its steady-state value which differs significantly from its thermal equilibrium. Since the order of magnitude of $\langle D \rangle_{\text{eq}}$ is depicted in Fig. 17(c) we have divided out its steady-state value D_∞ and also indicated the ratio $\langle D \rangle_{\text{eq}}/D_\infty$ as arrows on the right side with the same color to illuminate the short-time oscill-

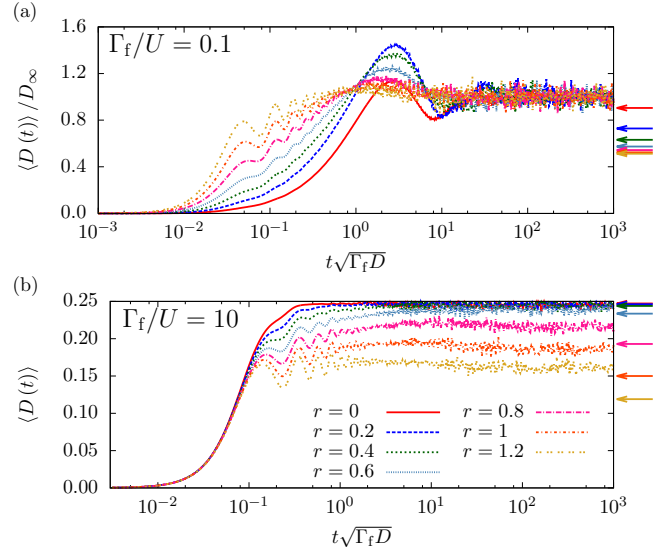


FIG. 18. (Color online) $\langle D(t) \rangle$ versus the dimensionless time $t\sqrt{\Gamma_f D}$ for different bath exponents r in hybridization quenches from $\Gamma_i = 0$ to (a) $\Gamma_f/U = 0.1$ and (b) $\Gamma_f/U = 10$ and fixed $D/U = 100$, and $U = U_i = U_f = \text{const}$. In (a) we divided $\langle D(t) \rangle$ by D_∞ (cf. Eq. (14)) to enlighten the oscillatory behavior independently of the absolute value of $\langle D(t) \rangle$. The equilibrium expectation values after the quench are marked by the arrows at the right side of the graph.

latory behavior independently of the absolute value of $\langle D(t) \rangle$. Due to the rescaling, the time scale $\tau = 1/\sqrt{\Gamma_f D}$ governing the overall response is not directly discernible as in Fig. 18 (b).

On an intermediate time scale, we observe a damped oscillatory behavior for small r . These oscillations are more strongly pronounced with increasing r due to a stronger concentrated local moment formation around the impurity, and therefore the local dynamics between the impurity and the first Wilson shell is more emphasized. The deviation of the equilibrated steady-state value and the thermodynamic equilibrium, indicated by the arrows on the right of the graph, is increasing with increasing r which is also correlated with the increasing localization of the effective moment.

For the weakly correlated regime, depicted in Fig. 18(b), we find thermalization only for quenches into the SC phase. For $1/2 < r$, the steady-state value of $\langle D(t) \rangle$ is reduced with increasing r , and the difference to the thermal equilibrium is also continuously increasing due to quenching into the LM phase. Plotting the data versus $t\sqrt{\Gamma_f D}$ clearly reveals the universal r -independent time scale governing the short-time dynamics, as predicted by our perturbation theory. For quenches remaining in the LM phase, we observe short-time oscillations whose damping decreases with increasing r . This oscillations have the same frequency dependency as in Fig. 18(a) proportional to the Coulomb repulsion U .

IV. CONCLUSION

We have analyzed in detail the impurity dynamics of the pg-SIAM after local quenches.

In Sec. III A we have summarized the known equilibrium properties of the pseudogap model. There we have discussed the limitations of a Gutzwiller ansatz [16, 17, 19, 20] which only allows a decoupling spin moment forming on the impurity site in the LM phase whereas the NRG is able to generate the correct ground state describing a spatially extended spin-moment formation.

We have distinguished two quench types: the interaction quench in Sec. III B and the hybridization quench in Sec. III C.

For the former we have found a universal curve for interaction quenches within the SC phase: All dependencies of the Coulomb repulsion U_f , the band width D , and the bath exponent r are included in the scaling function $f(t)$ defined by Eq. (11) and the crossover time scale t_{co} approximated by Eq. (13).

From the temperature-dependent effective moment $\mu_{\text{eff}}^2(T)$ in the LM regime we have defined the crossover scale T^* that depends on the distance $U - U_c$ and vanishes for U_c . Since T^* is directly related to the NRG iteration N^* beyond which the LM FP is approached, $1/T^*$ can be interpreted as a characteristic length scale of the local-moment formation: the larger T^* will be, the more localized the effective spin moment decoupling from the rest of system will be. Moreover, we have demonstrated that the difference between the steady-state value D_∞ and thermodynamic expectation value D_{eq} only depends on T^* independently of varying U_f at fixed D or varying D for fixed U_f . This spatial dependency of the decoupled moment encoded in the NRG ground state cannot be accounted for in the Gutzwiller approach [16] since the wave-function ansatz restricts the moment formation onto the impurity site.

In the presented hybridization quenches we always start from a decoupled impurity at $t = 0$ and switch on H_{hyp} with different coupling strength. For a small hybridization, the system remains in the LM phase while a large hybridization drives the system across the QCP into the SC phase. We have gauged the quality of our numerical results by our analytic second-order perturbation theory, which becomes exact for times $t \rightarrow 0$, and found excellent agreement between the analytics and the numerics in the applicability range of the perturbation theory. We could show that the short-time dynamics is governed by the time scale $1/\sqrt{\Gamma_f D}$ which is independent of the Coulomb interaction.

By comparison of our data with the recent Gutzwiller results [16] we could demonstrate the shortcomings of this variational ansatz that already strongly deviates from the asymptotically exact perturbative result for short-time scales. After illustrating the major difference of the physical content in the ground-state wave function between the approximate Gutzwiller approach and the exact NRG

ground state, the differences between the equilibrium as well as the nonequilibrium results of both methods become transparent.

Thermalization was observed within the errors of the TD-NRG [32, 44] for quenches within or into the SC phase. Due to the extended nature of the decoupling effective spin in the LM phase, we still found a steady-state value for $\langle D(t) \rangle$ that, however, increasingly deviates from the thermodynamic expectation value. Interestingly, we found a thermalization of the hybridization energy E_{hyb} which accounts for the major local energy change after the quench. We also provide a short overview for hybridization quenches for exponents $1/2 < r$ where only a LM FP is found for $U > 0$.

V. ACKNOWLEDGMENTS

We thank Florian Gebhard and Jörg Bünnemann for fruitful discussions on the nature of the Gutzwiller wave function for quantum impurity systems. We acknowledge financial support by the German-Israel Foundation through Grant No. 1035/2009 and by the Deutsche Forschungsgemeinschaft through AN 275/7-1. CPU time was partially granted by the NIC, FZ Jülich, under project No. HHB00.

Appendix A: Perturbation theory for hybridization quenches

In general, we assume that the system is in equilibrium for $t < 0$ and that its dynamics is governed by the initial Hamiltonian H_0 which is switched to $H_f = H_0 + H_p$ by the additional perturbation H_p .

The real-time dynamics of any operator \hat{O} can be calculated using a time-dependent density operator $\hat{\rho}(t)$,

$$\langle O(t) \rangle = \text{Tr} \left\{ \hat{\rho}(t) \hat{O} \right\} = \text{Tr} \left\{ \hat{\rho}^I(t) \hat{O}^I(t) \right\} \quad (\text{A1})$$

where we have transformed all the operators into the interaction picture $\hat{O}^I(t) = \exp(iH_0 t) \hat{O} \exp(-iH_0 t)$ in the last step.

The time evolution of the density operator is calculated by integrating the von Neumann equation

$$\frac{\partial \hat{\rho}^I}{\partial t} = i[\hat{\rho}^I(t), H_p^I(t)] \quad (\text{A2})$$

to

$$\hat{\rho}^I(t) = \hat{\rho}_0 + i \int_0^t d\tau_1 [\hat{\rho}^I(\tau_1), H_p^I(\tau_1)] \quad (\text{A3})$$

where we have used the boundary condition $\hat{\rho}^I(0) = \hat{\rho}_0 = \exp(-\beta H_0)/Z_0$ and $Z_0 = \text{Tr} \{ \exp(-\beta H_0) \}$.

Iterating Eq. (A3) once more and substituting the expression into (A1) the time evolution of an expectation

value up to second order of the perturbation is given by the general expression

$$\begin{aligned} \langle O(t) \rangle \approx & \text{Tr} \left\{ \hat{\rho}_0 \hat{O} \right\} + i \int_0^t d\tau_1 \text{Tr} \left\{ \hat{\rho}_0 [H_p^I(\tau_1), \hat{O}^I(t)] \right\} \\ & - \int_0^t d\tau_1 \int_0^{\tau_1} d\tau_2 \text{Tr} \left\{ \hat{\rho}_0 [H_p^I(\tau_2), [H_p^I(\tau_1), \hat{O}^I(t)]] \right\}. \end{aligned} \quad (\text{A4})$$

For a hybridization quench, we start with a decoupled impurity and switch on the hybridization $H_p = H_{\text{hyb}}$ at $t = 0$. Although the Hamiltonian

$$H_0 = \sum_{\sigma k} \epsilon_k c_{\sigma k}^\dagger c_{\sigma k} + \sum_{\sigma} \epsilon_d d_{\sigma}^\dagger d_{\sigma} + U d_{\downarrow}^\dagger d_{\downarrow} d_{\uparrow}^\dagger d_{\uparrow} \quad (\text{A5})$$

is not bilinear, it can be diagonalized exactly and all expectation values with respect to $\hat{\rho}_0$ are known. The transformation of H_{hyb} into the interaction picture only requires

$$c_{\sigma k}^I(t) = c_{\sigma k} e^{-i\epsilon_k t}, \quad c_{\sigma k}^{\dagger I}(t) = c_{\sigma k}^\dagger e^{i\epsilon_k t} \quad (\text{A6})$$

and

$$d_{\sigma}^I(t) = |0\rangle \langle \sigma| e^{-i\epsilon_d t} - \sigma | -\sigma \rangle \langle 2| e^{-i(\epsilon_d + U)t}, \quad (\text{A7})$$

$$d_{\sigma}^{\dagger I}(t) = |\sigma\rangle \langle 0| e^{i\epsilon_d t} - \sigma |2\rangle \langle -\sigma| e^{i(\epsilon_d + U)t}. \quad (\text{A8})$$

Now we specialize to a particle-hole symmetric model, $\epsilon_d = -U/2$ and $n_{\sigma} = 1/2$. For $T \rightarrow 0$, the initial double occupancy $\text{Tr} \left\{ \hat{\rho}_0 \hat{D} \right\} = 0$; likewise also the first-order contribution in Eq. (A4) vanishes since $\text{Tr} \left\{ \hat{\rho}_0 [H_{\text{hyb}}^I(t), \hat{D}] \right\} = 0$.

After evaluating the commutators and the traces of the second-order contribution for $T \rightarrow 0$, we are left with

$$\langle D(t) \rangle = \sum_k V_k^2 f(\epsilon_k) (I^+(\epsilon_k) + I^-(\epsilon_k)) \quad (\text{A9})$$

where the two integrals

$$\begin{aligned} I^{\pm}(\epsilon_k) = & \int_0^t dt_1 \int_0^{t_1} dt_2 e^{\pm i(\epsilon_k - \epsilon_d - U)t_2} \\ & \times e^{\mp i(\epsilon_k - \epsilon_d - U)t_1} \end{aligned} \quad (\text{A10})$$

can be evaluated analytically.

Using the pseudogap density of states we rewrite the sum over k as an integral over ϵ ,

$$\langle D(t) \rangle = \int_{-D}^D \Gamma(\epsilon) \frac{f(\epsilon) [1 - \cos((\epsilon - \epsilon_d - U)t)]}{(\epsilon - \epsilon_d - U)^2} d\epsilon \quad (\text{A11})$$

which requires numerical evaluation.

For $T \rightarrow 0$, we can perform the integration analytically in a series expansion and obtain the final result

$$\begin{aligned} \langle D(t) \rangle = & \frac{\Gamma_0 D}{\pi} t^2 + \frac{2\Gamma_0(1+r)}{\pi} \sum_{n=2}^{\infty} \frac{(-1)^{2n}}{(2n)!} \\ & \times \int_{-D}^0 \left| \frac{\epsilon}{D} \right|^r ((\epsilon - \epsilon_d - U)t)^{2n} d\epsilon. \end{aligned} \quad (\text{A12})$$

-
- [1] J. M. Elzerman, R. Hanson, L. H. W. van Beveeren, B. Witkamp, L. M. K. Vandersypen, and L. P. Kouwenhoven, *Nature* **430**, 431 (2004).
 - [2] P. W. Anderson, *Phys. Rev.* **124**, 41 (1961).
 - [3] H. R. Krishna-murthy, J. W. Wilkins, and K. G. Wilson, *Phys. Rev. B* **21**, 1003 (1980); **21**, 1044 (1980).
 - [4] R. Bulla, T. A. Costi, and T. Pruschke, *Rev. Mod. Phys.* **80**, 395 (2008).
 - [5] R. Bulla, T. Pruschke, and A. C. Hewson, *Journal of Physics: Condensed Matter* **9**, 10463 (1997).
 - [6] C. Gonzalez-Buxton and K. Ingersent, *Phys. Rev. B* **57**, 14254 (1998).
 - [7] M. T. Glossop and D. E. Logan, *Journal of Physics: Condensed Matter* **15**, 7519 (2003).
 - [8] M. Vojta, *Philosophical Magazine* **86**, 1807 (2006).
 - [9] D. Withoff and E. Fradkin, *Phys. Rev. Lett.* **64**, 1835 (1990).
 - [10] K. Chen and C. Jayaprakash, *Journal of Physics: Condensed Matter* **7**, L491 (1995).
 - [11] K. Ingersent, *Phys. Rev. B* **54**, 11936 (1996).
 - [12] K. G. Wilson, *Rev. Mod. Phys.* **47**, 773 (1975).
 - [13] F. B. Anders and A. Schiller, *Phys. Rev. Lett.* **95**, 196801 (2005).
 - [14] F. B. Anders and A. Schiller, *Phys. Rev. B* **74**, 245113 (2006).
 - [15] H. T. M. Nghiem and T. A. Costi, *Phys. Rev. B* **89**, 075118 (2014).
 - [16] M. Schiró, *Phys. Rev. B* **86**, 161101 (2012).
 - [17] M. C. Gutzwiller, *Phys. Rev.* **137**, A1726 (1965).
 - [18] T. Schickling, F. Gebhard, J. Bünnemann, L. Boeri, O. K. Andersen, and W. Weber, *Phys. Rev. Lett.* **108**, 036406 (2012).
 - [19] G. Seibold and J. Lorenzana, *Phys. Rev. Lett.* **86**, 2605 (2001).
 - [20] N. Lanatà and H. U. R. Strand, *Phys. Rev. B* **86**, 115310 (2012).
 - [21] L. Fritz and M. Vojta, *Reports on Progress in Physics* **76**, 032501 (2013).
 - [22] P.-W. Lo, G.-Y. Guo, and F. B. Anders, *Phys. Rev. B* **89**, 195424 (2014).
 - [23] L. Fritz and M. Vojta, *Phys. Rev. B* **70**, 214427 (2004).
 - [24] M. Vojta and L. Fritz, *Phys. Rev. B* **70**, 094502 (2004).
 - [25] I. Schneider, L. Fritz, F. B. Anders, A. Benlagra, and M. Vojta, *Phys. Rev. B* **84**, 125139 (2011).
 - [26] P. Mazur, *Physica* **43**, 533 (1969).
 - [27] M. Suzuki, *Physica* **51**, 277 (1971).

- [28] G. S. Uhrig, J. Hackmann, D. Stanek, J. Stolze, and F. B. Anders, Phys. Rev. B **90**, 060301 (2014).
- [29] A. Rosch, Eur. Phys. J. B **85**, 6 (2012).
- [30] T. Kanao, H. Matsuura, and M. Ogata, Journal of the Physical Society of Japan **81**, 063709 (2012).
- [31] M. Vojta, L. Fritz, and R. Bulla, Europhys. Lett. **90**, 27006 (2010).
- [32] E. Eidelstein, A. Schiller, F. Güttge, and F. B. Anders, Phys. Rev. B **85**, 075118 (2012).
- [33] T. A. Costi, A. C. Hewson, and V. Zlatic, J. Phys.: Condens. Matter **6**, 2519 (1994).
- [34] R. Peters, T. Pruschke, and F. B. Anders, Phys. Rev. B **74**, 245114 (2006); A. Weichselbaum and J. von Delft, Phys. Rev. Lett. **99**, 076402 (2007).
- [35] N. Lanatà, Phys. Rev. B **82**, 195326 (2010).
- [36] The precise mathematical definition of T^* will be given in Sec. III B 2.
- [37] V. Barzykin and I. Affleck, Phys. Rev. Lett. **76**, 4959 (1996).
- [38] V. Barzykin and I. Affleck, Phys. Rev. B **57**, 432 (1998).
- [39] I. Affleck and P. Simon, Phys. Rev. Lett. **86**, 2854 (2001).
- [40] E. S. Sørensen and I. Affleck, Phys. Rev. Lett. **94**, 086601 (2005).
- [41] I. Affleck, L. Borda, and H. Saleur, Phys. Rev. B **77**, 180404 (2008).
- [42] B. Lechtenberg and F. B. Anders, Phys. Rev. B **90**, 045117 (2014).
- [43] T. Chowdhury and K. Ingersent, arXiv:1410.5546 (2014).
- [44] F. Güttge, F. B. Anders, U. Schollwoeck, E. Eidelstein, and A. Schiller, Phys. Rev. B **87**, 115115 (2013).
- [45] P. Reimann, Phys. Rev. Lett. **101**, 190403 (2008).
- [46] M. Rigol and M. Srednicki, Phys. Rev. Lett. **108**, 110601 (2012).
- [47] J. R. Schrieffer and P. A. Wolff, Phys. Rev. **149**, 491 (1966).
- [48] P. Nordlander, M. Pustilnik, Y. Meir, N. S. Wingreen, and D. C. Langreth, Phys. Rev. Lett. **83**, 808 (1999).